Characterisation of B-type stars in four young Galactic open clusters. II. Asteroseismology of pulsations in TESS light curves

F. Nardini[1], D. M. Bowman[1,2], J. Bodensteiner[3], P. Van Daele[1], L. J. A. Scott[1], J. Henneco[1], K. Thomson-Paressant[1], H. Sana[2,4]

[1] School of Mathematics, Statistics and Physics, Newcastle University, Newcastle upon Tyne, NE1 7RU, United Kingdom
[2] Institute of Astronomy, KU Leuven, Celestijnenlaan 200D, 3001 Leuven, Belgium
[3] Anton Pannekoek Institute for Astronomy, University of Amsterdam, 1090 GE Amsterdam, The Netherlands
[4] Leuven Gravity Institute, KU Leuven, Celestijnenlaan 200D, 3001 Leuven, Belgium

Accepted XXX. Received YYY; in original form ZZZ

ABSTRACT

Massive stars play a key role in the chemical and dynamical evolution of galaxies. Two of their most common properties, pulsations and binarity, can strongly influence both their internal structure and evolution. Young open clusters provide ideal laboratories to study these stars, since they are mostly coeval and chemically homogeneous environments. We analyse a sample of 82 B-type stars distributed among the Galactic open clusters h and χ Persei, NGC 457, NGC 581, and NGC 1960, with ages between 15 and 30 Myr. To extract light curves in these crowded fields, we use both simple aperture photometry and a novel point-spread-function-based method designed to minimise contamination in full-frame images from the Transiting Exoplanet Survey Satellite (TESS). With these approaches, we successfully extract light curves for 63 stars. We find that most stars in the sample exhibit photometric variability, showing that pulsations are a common property of B-type stars. We also confirm previous evidence that the majority of early B-type stars are in binary systems, indicating that the presence of pulsations does not significantly bias binary detection. Finally, we perform asteroseismic forward modelling of a gravity-mode pulsator in NGC 1960. We estimate the asteroseismic age of the star to be $\sim$ 50 Myr and compare it with the cluster age inferred from isochrone fitting, which is $\sim$ 30 Myr. We discuss the implications of the differences between these age estimates in terms of stellar modelling uncertainties and the potentially distinct evolutionary behaviour of rapidly rotating stars in clusters.

Key words: asteroseismology - stars: binaries: spectroscopic - stars: early-type - stars: emission-line, Be - stars: oscillations - stars: rotation

1 INTRODUCTION

In recent years, our understanding of the physical processes that govern stellar structure and evolution has largely improved (see Kippenhahn et al. 2013, for a monograph). However, we still lack a complete understanding, especially in predicting the end product of a single, isolated massive star. That is because of the variety of physical processes in their lives, from strong stellar winds, high rotation rates that influence the internal mixing, and potentially magnetic fields (Langer 2012). For example, large theoretical uncertainties exist in stellar evolution models for mixing, both due to rotation and other instabilities related to convective boundaries, which play a crucial role in the mass of the helium core, the main-sequence lifetime, and subsequent evolution (Talon et al. 1997; Johnston 2021). Moreover, most massive stars are born and eventually interact with at least one companion in binary systems (Sana et al. 2012; de Mink et al. 2014; Offner et al. 2023). These interactions, such as mass transfer and tides, introduce additional complications and can even lead to mergers (see Marchant & Bodensteiner 2024; Schneider 2025, for recent reviews).

Asteroseismology is a powerful tool that allows us to constrain the structure of stars across the Hertzsprung–Russell (HR) diagram (Aerts et al. 2010) using stellar pulsations. For example, the asteroseismic analysis of massive stars has allowed us to estimate their interior rotation and mixing profiles (Aerts et al. 2003; Dupret et al. 2004; Vanlaer et al. 2025; Fritzewski et al. 2025), and even constrain their interior magnetic fields (e.g. Lecoanet et al. 2022; Vandersnickt et al. 2025). Modern space telescopes, such as MOST (Walker et al. 2003), CoRoT (Auvergne et al. 2009), BRITE (Weiss et al. 2014), Kepler/K2 (Borucki et al. 2010; Howell et al. 2014), and the ongoing TESS mission (Ricker et al. 2015) have shown that almost all massive stars in the Galaxy pulsate (e.g. Balona et al. 2011; Burssens et al. 2020). Moreover, a large fraction of massive stars in the low-metallicity Large and Small Magellanic Clouds exhibit photometric variability that probes their mass and age (Bowman et al. 2019, 2024; Ma et al. 2024). Massive stars are intrinsically rare compared to low-mass stars, and these space missions have provided the first high-precision, long-duration time-series data for a large sample of massive stars suitable for ensemble asteroseismology (see Bowman 2020, for a review). For massive stars in binary systems, which can be subject to mass transfer, mergers, and tidal forces, asteroseismol-

ogy is more complicated but provides valuable constraints on binary evolution theory (see Southworth & Bowman 2025, for a review).

Pulsations are typically characterised by their dominant restoring force. Gravity modes have buoyancy as the restoring force, while pressure modes have the pressure gradient as their main restoring force. In massive stars, pulsations can be excited by different mechanisms, including a heat-engine mechanism operating in local opacity bumps (κ mechanism) near the stellar surface (Dziembowski & Pamiatnykh 1993; Dziembowski et al. 1993; Miglio et al. 2007), stochastically excited gravity waves (see Bowman 2023, for a review) and tides in close binary systems (Southworth & Bowman 2025). It is usually not possible to identify the pulsation excitation mechanism purely from observations alone, since this requires non-adiabatic pulsation models (e.g. Townsend & Teitler 2013). However, since the κ mechanism excites coherent pulsation modes with long lifetimes and turbulent convection typically excites damped modes with short lifetimes, it is usually possible to distinguish between the two cases.

Among stars of spectral types O and B, there are three main pulsator types: slowly pulsating B-type stars (SPB), β Cephei stars, and stochastic low-frequency (SLF) variables. These are separated because of distinctions in their excitation mechanism and/or instability regions in the HR diagram. SPB stars have spectral types between B3 and B9 and typically have high-radial order gravity modes excited by the κ mechanism (Pápics et al. 2017; Szewczuk & Daszyńska-Daszkiewicz 2018; Szewczuk et al. 2021; Pedersen et al. 2021). At higher masses are the β Cep stars, which have birth masses approximately between 8 and 30 $M_\odot$ and typically show low-radial order pressure and gravity modes (Stankov & Handler 2005; Burssens et al. 2023; Fritzewski et al. 2025). The pulsation periods of SPB and β Cep stars are of order several hours to a few days. We note that it is possible to have so-called hybrid pulsators (Handler 2009), which are stars that show characteristics of different pulsator classifications. Historically, the term hybrid has been used to refer to stars with characteristics of both SPB and β Cep stars and located in the overlapping instability regions of the HR diagram, which are largely occupied by different classes of pulsators.

Another relevant group of pulsators among early-type stars are Be stars. Space-based photometry has demonstrated that non-radial pulsations are almost ubiquitous among Be stars (Rivinius et al. 2003; Semaan et al. 2018a; Labadie-Bartz et al. 2022). Both the light curves and the frequency spectra of pulsating Be stars are usually characterised by similar properties (e.g. complex beating patterns and frequency groups, Bradley et al. 2015; Kurtz et al. 2015). On longer time scales of months to years, Be stars experience epochs of brightening or fading, which are likely attributed to the dissipation or growth of an equatorial decretion disc created by mass ejections (Rivinius et al. 2013, 2016; Semaan et al. 2018b; Labadie-Bartz et al. 2025; Nova et al. 2025). Spectroscopically, classical Be stars are characterised by emission lines in their spectra caused by the presence of the equatorial decretion disc. It is thought that their rapid rotation rates are related to the presence of this circumstellar material (Rivinius et al. 2013; Rivinius & Klement 2026). The formation of a Be star, specifically if it was born as a single fast rotator or if it is a binary interaction product, is still debated in the literature (Hastings et al. 2020; Bodensteiner et al. 2020a).

The majority of massive stars are born in clusters or associations, and a major advantage of investigating binarity and pulsations in these systems is that open clusters share a common metallicity and age. This reduces the parameter space in subsequent modelling. Comparing multiple clusters spanning a range of ages allows an investigation of how the binary and pulsation properties of stars change in time. Recently, Nardini et al. 2025 (hereafter Paper 1) performed a spectroscopic characterisation of a sample of 74 early B stars in four young open clusters: h and χ Persei, NGC 457, NGC 581, and NGC 1960. The clusters were selected based on their ages to fill a gap in the literature from young to intermediate age: 15 Myr for h and χ Persei; 24 Myr for NGC 457; 29 Myr for NGC 581; and 30 Myr for NGC 1960 (Dias et al. 2021). High-resolution multi-epoch HERMES (Raskin et al. 2011) spectroscopy was used to identify binary systems based on radial velocity variability, and it was shown that no statistically significant differences occur in the binary fraction among the four clusters, with an overall bias-corrected binary fraction of 79^{+19}_{-16} per cent (see Paper 1). Knowing the cluster ages and assuming coeval evolution for stars in the same cluster provides a significant advantage, particularly when one of the goals is to identify candidates for pre- and post-interaction binary systems.

In this second paper, we characterise the photometric variability of this sample of early B-type main-sequence stars in four Galactic open clusters using new time-series space photometry from the NASA TESS mission (Ricker et al. 2015). We classify the different types of pulsators and use forward astereoseismic modelling to validate the reported cluster age of NGC 1960. In Sect. 2 we describe the sample, discuss the methods used to extract the light curves and for the frequency analysis, along with a discussion of the differences of the atmospheric parameters determined using two different methods. Section 3 describes the variability in the four clusters with a focus on pulsating Be stars, β Cep, SPBs and hybrids. In Sect.4 we discuss the asteroseismic analysis and the forward modelling of an SPB star in the cluster NGC 1960. Section 5 is about revisiting the binary systems and discussing the photometric binaries identified in the sample. Lastly, we give a summary and conclusions in Sect. 6.

2 METHODS

2.1 Sample selection

In this paper, we analyse a sample of 82 stars in four young open clusters: 26 are members of h and χ Persei, 19 are from NGC 457, 14 are from NGC 581, and 23 are from NGC 1960. This sample is slightly larger than the 74 B-type stars analysed spectroscopically in Paper 1. Here, we included the additional three members of the cluster h and χ Persei (h Per 0622, BD+56 515 and χ Per 2114) that lacked multi-epoch HERMES spectroscopy for the binary analysis in Paper 1. Additionally, five late-B stars (NGC 1960 3, NGC 1960 12, NGC 1960 14, NGC 1960 86 and NGC 1960 92), which span spectral types from B7 to B9, were not included in Paper 1 but included in this work to ensure better coverage of the full mass range of B-type stars in all four clusters. Figure 1 shows an asteroseismic HR diagram for all 82 stars in our combined four-cluster sample. The properties of the stars are reported in Table B1 (see also Sect. 2.5).

We note that the precise location of the main-sequence (MS) in Fig. 1 depends on the input physics and numerics used in theoretical evolutionary tracks, which affects any interpretation of whether a star can be considered to be on the MS. In our case, the evolutionary tracks shown in Fig. 1 were computed by Burssens et al. (2020) using the Modules for Experiments in Stellar Astrophysics (MESA; Paxton et al. 2011, 2013, 2015, 2018, , v.12115). These tracks assume non-rotating stars with Galactic metallicity $Z_{\rm ini} = 0.014$, an initial hydrogen abundance of $X_{\rm ini} = 0.71$, a diffusive exponential profile for convective boundary mixing (CBM) with $f_{\rm CBM} = 0.02$, and an envelope mixing coefficient of $\log D_{\rm mix} = 1.0$. Different implementations for rotation and mixing (e.g. more efficient mixing due to faster rotation) would shift the terminal age MS (TAMS) towards

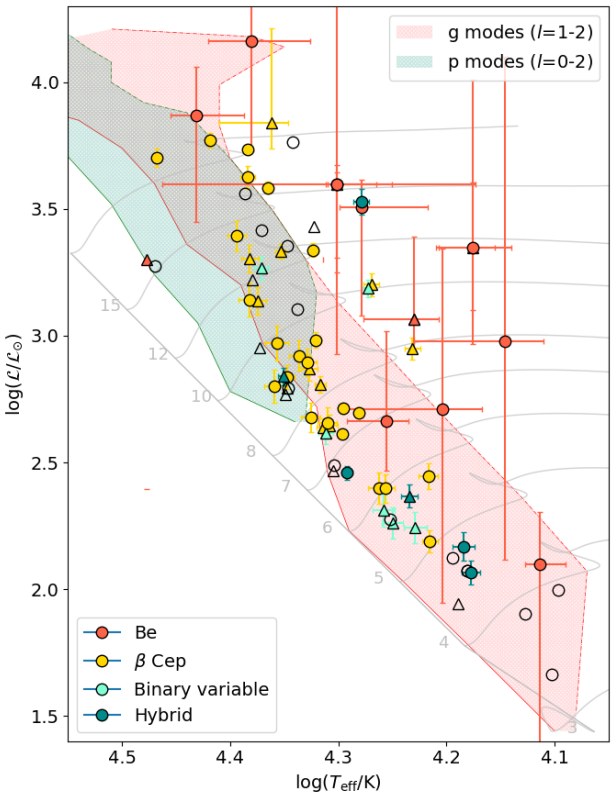

Figure 1. Asteroseismic HR diagram of the combined sample of 82 B-type stars across the four young open clusters studied in this work. We represent different classes of pulsators with different colours, and the markers indicate apparent single stars (circles) and binaries (triangles). Evolutionary tracks in units of $M_\odot$ and theoretical pulsation instability strips are from Burssens et al. (2020), for which the green shaded region is for pressure modes, and red is for gravity modes. The stellar parameters for non-emission line stars were determined using Gaia's ESP-HS module, whereas these were determined using a grid of TLUSTY (Hubeny & Lanz 1995; Lanz & Hubeny 2007) models for the Be stars.

cooler temperatures and increase the main-sequence lifetime (see Bowman 2020).

2.2 TESS light curve extraction

The NASA TESS space mission is an all-sky survey with the primary-mission objective being to detect exoplanets transiting bright stars (Ricker et al. 2015). The field of view is 24°×96° and TESS observes the entire sky in a series of observational sectors that last for at least 27 d. Originally launched in 2018, TESS is currently in its second extended mission and has returned to re-observe stars in multiple sectors, meaning that the total time span of its assembled light curves spans several years in most cases. This survey approach facilitates the discovery and follow-up asteroseismic analysis of many massive stars (see review by Bowman 2020).

Although working with open clusters provides the advantage of having a stellar sample of the same age and chemical composition, crowded fields are a major challenge when it comes to light curve extraction with the TESS mission (e.g. Bowman et al. 2024; Van Daele et al. 2026). Due to TESS's large pixel size (21 arcsec), blending and contamination are often inevitable for dense environments such as clusters. However, these limitations depend on the location of a star within the cluster and the proximity and brightness of other stars, thus each target has a different level of contamination.

2.2.1 *Simple aperture photometry*

TESS full-frame images (FFIs) are available with cadences of 30 min, 10 min, and 200 s for the nominal, first-extended and second-extended cycles, respectively, and are publicly available on MAST[1]. At the time of our analysis, TESS FFIs were available up to sector 85 for the clusters *h* and χ Persei and NGC 581, to sector 58 for NGC 457, and to sector 73 for NGC 1960. We used the LIGHTKURVE[2] package (Lightkurve Collaboration et al. 2018) together with TESSCUT (Brasseur et al. 2019) to download 20 × 20 pixel cutouts of the FFIs for each target. To extract light curves, we used simple aperture photometry (SAP) with three different aperture masks: a 1 × 1 pixel mask, a 3 × 3 mask, and an optimised mask selected interactively for each target by visual inspection to maximise the signal-to-noise ratio (S/N) of variability and minimise contamination (see discussion by Scott & Bowman 2026). The 1 × 1 pixel mask is a useful diagnostic tool to check if any detected variability originates from the target or from a neighbouring contaminating source. Meanwhile, whether the 3×3 or the interactive masks were better and thus used for subsequent analysis depends on the level of blending and contamination of each target. An example of the three different masks for χ Per 2296 and the resultant light curves is shown in Fig. 2.

To reduce these raw light curves, a background mask is constructed to include all pixels with flux levels below 0.5 per cent of the target star's flux, as these pixels contain mostly background light. These background-corrected light curves are then detrended using principal component analysis (PCA; Hotelling 1932). Detrending using PCA identifies and removes instrumental trends and systematics in the background-corrected light curves. The optimal number of principal components was determined by trialling different options and inspecting their behaviour over time. We selected only those components that did not display any periodic signals, ensuring that the detrending process would not introduce or remove any astrophysical variability in the output light curves. This approach has proven reasonable for massive stars (see e.g. Bowman et al. 2022; Scott & Bowman 2026). Finally, additional detrending was applied to all stars using a long-period spline fit with the `Python` SPLREP and SPLEV functions from SCIPY[3] to remove any sector-long trends missed by the PCA detrending.

2.2.2 *Contamination in crowded fields*

Light curve extraction is straightforward for targets that are isolated or only have nearby stars that are several magnitudes fainter. In these cases, using a 3 × 3 pixel mask was generally the best approach. However, for targets with a contaminating star of similar brightness within a few pixels, the interactive mask was deemed the best option since we can then manually select the pixels that maximise the target's flux and minimise the contaminating flux.

Table B1 includes a summary of the TESS light curve extraction results and the contamination ratio ($C_{\rm ratio}$) for all stars. This quantifies the amount of contamination based on the `Python` code TIC INSPECT[4],

[1] https://archive.stsci.edu/missions-and-data/tess
[2] https://github.com/lightkurve/lightkurve
[3] https://docs.scipy.org/doc/scipy/reference/interpolate.html
[4] https://github.com/mpaegert/tic_inspect

and is defined by Stassun et al. (2018) as $C_{\rm ratio} = F_{\rm n}/F_{\rm s}$, where the amount of flux from the neighbouring sources ($F_{\rm n}$) is divided by the flux of the target star ($F_{\rm s}$).

For 18 of our targets, there is a star of equal or higher brightness one pixel away from the central pixel. Therefore, even the 1×1 pixel mask option yields a large amount of contamination. This means that for such cases, we were able to tentatively assign them to a pulsator class, but we did not perform any further analysis. These objects are reported in Table B1 with daggers next to their variability class. Lastly, it was impossible to robustly extract a light curve at all for 19 targets, since another star with equal or lower magnitude is located in the same pixel. The median of the contamination ratio for these targets is 4, while for the 18 tentative targets is 2.3.

2.2.3 *PSF fitting*

For stars that were not completely isolated, but the contamination was not too high, we used the `Python` Lemons software developed by Van Daele et al. (2026). Lemons[5] performs light curve extraction using point spread function (PSF) fitting of TESS FFIs. In this approach, the flux of the target is extracted as a weighted sum of the pixel fluxes, where each pixel's weight is assigned according to the best-fit PSF assuming a 2D Gaussian. The Lemons software uses Gaia positions to locate stars and is further optimised for massive variable stars since it allows for variable centroid and broadness as fitting parameters for the target and nearby contaminating stars. This is important since the broadness of the PSF is time-dependent for a variable star. Furthermore, by allowing the centroid to vary from frame to frame, one compensates more robustly for the drift of the TESS spacecraft, which causes significant smearing of flux across the CCD during a TESS sector. Without mitigating this effect, PSF light curves include artificial long-term trends, especially for fainter stars ($T_{\rm mag} \gtrsim 12$).

Figure 2 includes an example in which the PSF light curve successfully demonstrates how contamination from a nearby eclipsing binary occurs for all of the 1×1, 3×3, and interactive pixel masks in the SAP methodology. In this particular example, all light curves obtained using the SAP masks show eclipses, which would lead to an incorrect classification for the target χ Per 2296. Using the PSF fitting, we mitigate the contaminating signal caused by the actual nearby eclipsing binary.

2.3 Photometric variability

Once the optimum light curve for each target had been determined from the SAP or PSF methods, we computed the discrete Fourier Transform (dFT) using the Period04 software (Lenz & Breger 2005). We calculated a dFT for each individual sector for each target to determine if the dominant frequencies were consistent across all sectors. Moreover, the large gaps (> 2 yr) between TESS cycles make frequency analysis of a combined light curve extremely challenging because of the complex spectral window (see Scott & Bowman 2026).

2.3.1 *Variability classification*

The different definitions of variability classes we used in this work are:

(i) β Cephei stars are dwarfs and giants with a spectral type of B3 or earlier, which show significant pulsation frequencies above about 4 $\rm d^{-1}$ (see Stankov & Handler 2005);

(ii) SPB stars are dwarfs with spectral type B2 or later that show significant pulsations below 4 $\rm d^{-1}$ (De Cat 2007);

(iii) Hybrids: dwarfs and giants with a spectral type later than B3 that show pulsations both above and below 4 $\rm d^{-1}$;

(iv) Pulsating Be stars are dwarfs showing emission in their spectra and pulsations in the light curves that typically form frequency groups in the amplitude spectrum (see Kurtz et al. 2015);

(v) Photometric binaries are targets that show either eclipses or ellipsoidal variability in their light curves due to binarity (see Southworth & Bowman 2025);

(vi) Rotational modulation stars show periodic modulation in their light curves commensurate with their rotation period, which is likely caused by chemical abundance spots;

(vii) δ Scuti stars are those with with spectral type later than B7 and that show significant pulsation frequencies above 40 $\rm d^{-1}$ (see Bowman & Kurtz 2018);

(viii) constant stars show no signs of variability in their light curve.

Note that these classification categories are not mutually exclusive. For example, some photometric binaries also exhibit pulsational variability. However, in this work, we classify stars based on their dominant photometric variability. The results of our photometric variability classification are shown in Table B1.

Variability classification was performed for the subset of 63 stars that are not heavily contaminated ($C_{\rm ratio} \leq 1$), with the frequency range of observed variability and the spectral type being the main criteria to distinguish different categories. For the remaining 19 stars, the contamination was deemed too high to reliably determine their variable classification. We discuss each class of pulsators in Section 3, and discuss the photometric binaries in Section 5.

2.3.2 *Inclination-radius-velocity relation*

For stars that show rotational modulation, we used the projected rotational velocities from Paper 1 (available for all stars except the SB2 systems) to estimate the rotation frequency range, assuming $\sin i$ between 0.1 and 1. The rotation frequency in $\rm d^{-1}$ is given by:

$$f_{\rm rot} \approx 0.02\, {\rm v_{rot}}\, ({\rm R_\odot}/R), \quad (1)$$

where $\rm v_{rot}$ is the equatorial rotational velocity in $\rm km\,s^{-1}$ and R is the stellar radius in solar radii. Estimates for the stellar radii were adopted from the tabulated values determined with different methods (eclipsing binaries and non-radial oscillations) by Gray (2021) and are reported in Table 1.

For the giant stars, we adopted the same radii as those used for dwarfs of the corresponding spectral types, as no reliable empirical or theoretical radius calibrations are available specifically for these evolved stars. This approximation is justified by the fact that, within a given spectral type, the radius variation between main-sequence and more evolved phases is significantly smaller than the uncertainties introduced by the inclination and the projected rotational velocity. To assess the impact of this assumption, we examined the difference in radius between the zero-age main sequence (ZAMS) and TAMS using the grids of MESA models from Johnston et al. (2019a). We considered B1- and B2-type stars (initial masses of 12 and 7 $\rm M_\odot$, respectively), and used the lowest and the highest values of the exponential convective boundary mixing (CBM, 0.005 and 0.04) available in the model grid. The stellar radius increases by approximately a

[5] https://github.com/pieterjanv314/Lemons

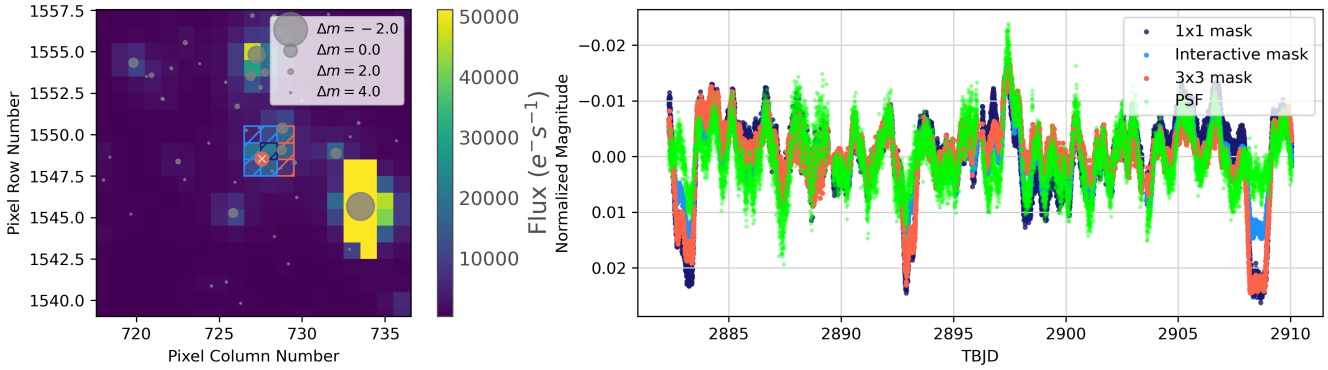

Figure 2. Example of the light curve extraction methodology for sector 58 of χ Per 2296. The left panel shows the 20×20 pixel cut-out of the TESS FFI with the target star in the centre. The different coloured hatched areas are the different aperture masks: 3×3 (red), interactive (light blue), and 1×1 (dark blue). The position of the target and neighbouring stars was determined using the Python package TPFPLOTTER (`https://github.com/jlillo/tpfplotter` Aller et al. 2020), which overplots the Gaia DR3 catalogue over the TESS TPF, and the size of the points is proportional to their TESS magnitude. The right panel shows the different light curves extracted with the different aperture masks in the corresponding colours. Additionally, the PSF light curve extracted using the LEMONS software (Van Daele et al. 2026) is shown in green, which demonstrates that the eclipses do not originate from the target.

Table 1. Approximate radii for dwarf B-type stars from Gray (2021).

SpT	R[$R_\odot$]
B0	6.50
B1	4.75
B2	4.20
B3	3.50
B5	2.69
B7	2.44
B9	2.07

factor of two from ZAMS to TAMS for the lowest CBM efficiency, and up to a factor of three for the highest CBM efficiency case. Given that our classification does not distinguish sub-giant or giant evolutionary stages within each spectral subtype, and that the amount of CBM is unknown, this level of uncertainty is acceptable for the purpose of this work.

2.4 Frequency analysis

For frequency analysis, we used TESS sectors with a 200-sec cadence, which are those from the second extended mission, unless two or more consecutive sectors were available in earlier sectors. For example, stars in NGC 1960 had three consecutive sectors with a 10-min cadence (i.e. sectors 43, 44 and 45).

For isolated stars, those with $C_{\rm ratio} \leq 1$, identified as β Cep, hybrids, and SPB stars, we identify significant frequencies using standard iterative pre-whitening methods (see Pápics 2012; Bowman & Michielsen 2021) using the longest uninterrupted chain of TESS sectors of the extracted and reduced light curves (see Section 2.2). The iterative prewhitening is achieved using the PERIOD04 software (Lenz & Breger 2005). Following Baran & Koen (2021), we adopt a significance threshold of S/N ≥ 4.6 in the amplitude spectrum, which corresponds to a false-alarm probability of approximately 0.1%. This is better suited for space-based observations, since the large number of data points and longer time spans compared to typical ground-based data sets require a higher S/N threshold. The noise is calculated from a frequency window of width 2 d^{-1} centred on the extracted frequency.

Following this, we checked for unresolved frequencies in the frequency lists of all stars. According to the Loumos–Deeming resolution criterion (Loumos & Deeming 1978), two frequencies are resolved if:

$$|f_j - f_k| \geq \frac{2.5}{\Delta T}\,, \tag{2}$$

where f_i and f_j are a pair of significant frequencies, and ΔT is the time span of the light curve. In instances where the criterion was not satisfied, the lower-amplitude frequency was discarded.

The next step was the identification of harmonics and combination frequencies. A frequency, f_i, is classed as a harmonic or a combination if:

$$|f_i - (mf_j - nf_k)| \leq \frac{2.5}{\Delta T}\,, \tag{3}$$

where f_j and f_k are the parent frequencies and $\{n, m\} \in \{0, \pm1, \pm2, \pm3\}$ (see Pápics 2012; Bowman 2017). The two highest-amplitude frequencies are considered parent frequencies and assumed to be self-excited pulsation mode frequencies (Kurtz et al. 2015), and the combination frequencies are then determined using Eq. 3. Since harmonic and combination frequencies may not represent independent self-excited pulsation modes and are generally not used in asteroseismic modelling (see discussion by Bowman 2017), they are not included in the final list of significant and independent pulsation frequencies for each star.

Appendix Table B2 reports the significant independent frequencies along with their amplitudes and phases for each pulsating star. Interesting pulsating stars are discussed in Section 3.

2.5 TLUSTY vs Gaia ESP-HS atmospheric parameters

In Paper 1, the atmospheric parameters were determined for apparently single stars and SB1 systems using a grid of rotationally broadened TLUSTY models (Hubeny & Lanz 1995; Lanz & Hubeny 2007). Using a similar approach to that used by Bodensteiner et al. (2023), a grid-based search of BSTAR2006 TLUSTY models and a χ^2 minimisation, the best-fitting projected rotational velocity was determined for each star. Only specific lines were used in the fitting process, especially for Be stars. In cases where emission was present in a star's spectrum, only the wings of the Balmer lines and metal lines were used in the fit, since these were least affected by emission.

In Paper 1, the distributions of projected rotational velocity were found to be statistically consistent across the four clusters.

In this work, we compare the values determined using the TLUSTY grid in Paper 1 with those derived by the Extended Stellar Parametrizer for Hot Stars (ESP-HS; Fouesneau et al. 2023; Frémat 2024) catalogue from data release 3 (DR3) of ESA's Gaia mission (Gaia Collaboration et al. 2016a,b, 2018, 2023). The ESP-HS module is applied to O-, B-, and A-type stars only after the source has been identified as a hot star by the Extended Stellar Parametrizer for Emission-Line Stars (ESP-ELS), which classifies both spectral type and the presence of emission lines. The ESP-HS module uses Gaia's BP/RP low-resolution spectra and, when available, the medium-resolution Radial Velocity Spectrometer (RVS) data. Stellar parameters are inferred by minimising the weighted squared residuals against synthetic spectral libraries. When RVS spectra of sufficient quality are available, their weighted squared residuals are included in the fit (Fouesneau et al. 2023; Frémat 2024).

Fouesneau et al. (2023) compared their astrophysical parameters obtained with the ESP-HS pipeline with several previous catalogues of early-type stars. They found good agreement in $T_{\rm eff}$ below 25 000 K, but a systematic underestimation of the Gaia values compared to spectroscopy above this temperature. Likewise, the scatter in the log g differences between Gaia and the reference catalogues increases from about 0.2 dex for A-type stars to roughly 0.4 dex for O-type stars. Furthermore, Shi et al. (2023) report that the Gaia $T_{\rm eff}$ values obtained by ESP-HS are reliable for pulsating hot main-sequence stars. They compared the ESP-HS derived parameters with those from low-resolution LAMOST spectra (Guo et al. 2021), and found that the effective temperatures from Gaia's ESP-HS catalogue are consistent for stars with $T_{\rm eff} \lesssim 30\,000$ K. The authors report only the effective temperature and mention that the consistency between the LAMOST stellar parameters (likely the surface gravity and the projected rotational velocity) and the ESP-HS parameters is poor, and therefore, they do not mention them in their papers.

The ESP-HS module of the Gaia mission has several limitations. For example, not all Be stars are correctly identified by ESP-ELS, meaning those misclassified as non-emission-line stars have unreliable stellar parameters. Of the 15 Be stars in our sample identified as such in Paper 1, only six are correctly classified as emission-line stars by ESP-ELS. Moreover, a similar problem arises for SB2 systems in that the spectral resolution of Gaia's RVS instrument is insufficient to detect two sets of spectral lines in most SB2 systems. Yet, since the flux of both components is present in the Gaia spectra, the derived atmospheric parameters are typically not reliable. Additionally, it is worth noting that stellar parameters from the Gaia ESP-HS catalogue are not available for five stars in our sample.

In Fig. 3 we show the spectroscopic HR diagrams of the four clusters, which use spectroscopic luminosity defined as $\mathcal{L} = T_{\rm eff}^4/g$ (Langer & Kudritzki 2014) as the ordinate axis. We compare the stellar parameters derived from the χ^2 minimisation procedure using TLUSTY models with those obtained by the ESP-HS module from the Gaia mission. The older cluster NGC 1960 (30 Myr; Dias et al. 2021) is dominated by late-B stars, and we find a smaller disagreement between our TLUSTY parameters and those from Gaia. The average absolute difference for the effective temperature is $\sim$ 2000 K, while for the surface gravity is $\sim$ 0.25 dex. The largest discrepancy appears in h and χ Per, which is the youngest cluster (15 Myr; Dias et al. 2021) and hosts the most massive stars in our sample. For example, our TLUSTY results tend to place these stars beyond the terminal-age main sequence (TAMS) in Fig. 3, which is likely because the TLUSTY approach has underestimated the log g values. This thus causes the spectroscopic luminosity to be overestimated. The average absolute differences are also larger compared to the older cluster: while the difference in $T_{\rm eff}$ is $\sim$ 3500 K, the difference in log g is $\sim$ 0.4 dex.

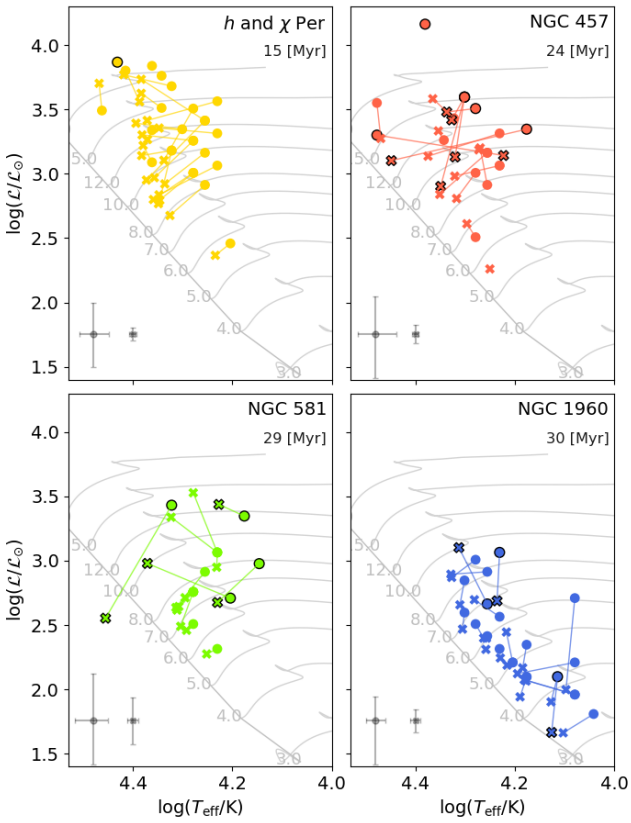

Figure 3. Spectroscopic HR diagrams of the four clusters. Circles indicate the stellar parameters obtained using the TLUSTY atmospheric models by Paper 1, while crosses indicate values from the Gaia ESP-HS catalogue. The Be stars are denoted by those with a black edge colour. The grey lines are stellar evolutionary tracks, which are labelled in units of $M_\odot$ and were computed by Burssens et al. (2020). The size of typical error bars for each cluster is shown in the bottom left, both for the TLUSTY (left) and for the ESP-HS (right). The ages reported below the name of each cluster in each panel are from Dias et al. (2021).

All Be stars in our sample show a particularly substantial discrepancy in their TLUSTY and Gaia parameters. This is expected because most of them are misclassified as non-emission-line objects by the Gaia mission and have subsequently been treated as non-emission-line B stars. For this reason, the parameters determined by the TLUSTY grid were used for the Be stars as well as for the five stars that do not have ESP-HS parameters, while for the remaining of the sample we used the ESP-HS parameters. On the other hand, our TLUSTY analysis of Be stars suffers from limitations of neglecting the effects of fast rotation and time-dependent emission features. Therefore, it is not surprising that the parameters of such stars have large uncertainties and a large discrepancy with the Gaia parameters.

3 VARIABILITY IN THE FOUR OPEN CLUSTERS

We use the TESS light curves and frequency spectra to classify the photometric variability of the 63 stars out of 82 with an acceptable level of contamination in our sample across the four clusters. The results of the variability classification are reported in the last column of Table B1. Among the 63 stars, 31 are β Cephei stars, 14 are

pulsating Be stars, seven are hybrids, five are photometric binaries, three are rotational modulation stars, one is a δ Scuti star, and two are constant. Based on the sample of 82 stars, we find a photometric variability fraction of 77 ± 5 per cent, but if only the stars not in crowded regions are considered (63), we obtain a variability fraction of 97 ± 2 per cent and a pulsator fraction of 84 ± 5 per cent. This demonstrates a high incidence of pulsations for early-type stars in young open clusters.

In the following sub-sections, we discuss each class of pulsators, highlighting interesting objects.

3.1 Pulsating Be stars

The photometric and spectroscopic variability characteristics of Be stars in the literature are detected in all of the Be stars analysed in this work. These include complex beating patterns in their light curves and multi-periodic non-radial gravity modes, that can form frequency groups due to the harmonics and combination frequencies (Kurtz et al. 2015). These features are common but not exclusive to Be stars, and are also generally found in rapidly rotating stars (Saio 2013; Kurtz et al. 2015; Nazé et al. 2024).

In Paper 1, a total of 15 Be stars were identified in multi-epoch Hermes spectroscopy, and in this work, 14 of them show pulsations in their TESS light curves. Only one of these 15, V* V1122 Cas, is too contaminated to determine whether the star is pulsating or if a nearby contaminating star is instead. Specifically, there is a variable blue supergiant in the same TESS FFI pixel of V* V1122 Cas, whose stochastic variability dominates over the variability of the Be star. Three Be stars (NGC 457 6, NGC 457 14, NGC 1960 47) are tentatively classified as pulsators, because there is considerable sector-to-sector variability in their light curves, indicating they are also likely contaminated. This means we cannot reliably perform any frequency analysis since it is not clear if the changes are due to stellar variability, contamination or instrumental effects. For the remaining 11 Be stars, the amount of contamination was low so it was possible to extract TESS light curves, calculate frequency spectra and perform iterative pre-whitening. Figure 4 shows the light curves, the frequency spectra, and the Hermes spectra zoomed on Hα for the 11 pulsating Be stars across the four clusters. The grey shaded region in each of the central panels marks the estimated frequency range in which one may expect rotational modulation, which is calculated using Eq. (1).

We detect multi-periodic gravity-mode pulsations in all 11 non-contaminated Be stars across the four clusters. For all of them, the peak with the highest amplitude has a frequency below 3 d^{-1}. Almost all of the stars in the sample show two or more frequency groups in their frequency spectra, which are consistent in frequency across all available sectors but vary in amplitude as expected. Frequency groups extending beyond 4 d^{-1} are only observed for the faster rotating Be stars ($v \sin i > 200$ km s^{-1}; shown in the bottom four rows of Fig. 4). This may lead to an incorrect classification of these four stars (NGC 457 91, NGC 581 49, NGC 1960 27, and EM* GGA 56) as β Cep stars because of the higher pulsation frequencies, but their rapid rotation can shift the gravity modes to higher frequencies (Labadie-Bartz et al. 2022; Aerts & Tkachenko 2024).

In terms of binarity, Be stars generally show a lack of main-sequence companions (Bodensteiner et al. 2020a), so it is not surprising that in this work only two Be stars are candidate binary systems (NGC 457 91 and NGC 1960 27). However, this does not exclude the possibility of companions being either a stripped star or a compact object (see e.g. Abdul-Masih et al. 2020; Shenar et al. 2020; Bodensteiner et al. 2020b). The presence of a companion might influence the decretion disc of a Be star, and cause the so-called violet-to-red (V/R) cycles attributed to density waves propagating through the disc (Rivinius et al. 2016). The binarity status of NGC 457 91 and NGC 1960 27 is discussed in more detail in Section 5.

Making a comparison or ensemble analysis is challenging since the Be phenomenon is transient and the stars in our sample show a different range of behaviours. Each individual pulsating Be star is discussed in the Appendix Sect.A1.

3.2 β Cep stars, SPB stars, and hybrids

Traditionally, β Cep stars have spectral types from O9 to B2 on the main sequence (Stankov & Handler 2005), corresponding to masses of about 8 to 25 M$_\odot$. However, modern space photometry has revealed that the low-radial order pressure and gravity modes of β Cep stars are found among both higher and slightly lower masses (Burssens et al. 2020; Fritzewski et al. 2025). The pressure-mode instability region from Burssens et al. (2020) has a minimum mass of about 8 M$_\odot$ and yet, although rare, some β Cep stars have been found to have masses as low as 5-6 M$_\odot$ (e.g. Burssens et al. 2019). In our sample, we find β Cep stars spanning almost the full mass range, from about 5 to about 25 M$_\odot$ with the lowest-mass β Cep stars being located outside the pressure-mode instability region, as shown in Fig. 1. For example, NGC 457 34, NGC 1960 87, and NGC 1960 91 have spectral types of B5 and atmospheric parameters that confirm them to be quite cool for β Cep stars.

On the other hand, distinguishing pressure modes from gravity modes in mid-B stars is challenging when relying solely on the observed frequency range. Some pulsators exhibit two distinct sets of self-excited pulsation spectra, where each set corresponds to modes typically associated with different established classes of variable stars. Such objects are therefore commonly referred to as hybrid pulsators (Handler 2009). The simultaneous presence of pressure and gravity modes for stars across a range of spectral types suggests For this reason, we classify β Cephei stars as early-B stars showing predominantly high-frequency ($f \geq 4$ d^{-1}) pulsations, while stars of spectral type B5 or later exhibiting low-frequency variability are classified as SPB stars or, when both frequency domains are present, as hybrids.

Overall, we find that β Cep are the most common class of pulsators in the sample, which is not unexpected considering it is dominated by early-B stars. However, two clear examples of SPB stars exist (NGC 1960 81 and NGC 1960 91), which have higher frequency gravity modes and frequency groups because of their rapid rotation. Figures 5 and 6 show the TESS light curves and frequency spectra of the 20 non-contaminated β Cep stars and hybrids, while Fig. 7 shows the light curves and dFTs of the two SPB. We classify two stars as hybrids: NGC 457 34 and NGC 1960 87 on the basis that their pulsation frequencies span a wide range in frequency and their spectral type places them in the overlapping region for pressure and gravity modes (c.f. Fig. 1). The remaining 18 stars include six in h and χ Persei, five in NGC 457, two in NGC 581 and 5 in NGC 1960. We emphasise that the somewhat lower number of pulsators in NGC 581 is likely due to the high crowding of the field rather than an intrinsically lower pulsator fraction. For most stars with one TESS sector, we find significant frequencies up to 8 d^{-1} with a few exceptions with higher frequencies (e.g. NGC 457 8, h Per 0843, h Per 0864, and BD+56 515). For stars in NGC 1960 and their longer TESS light curves of three consecutive sectors, we find significant frequencies up to about 30 d^{-1} (e.g. NGC 1960 38).

Unsurprisingly, due to their fast rotation rates, we did not detect any symmetric rotational splitting for any of the β Cep stars, which

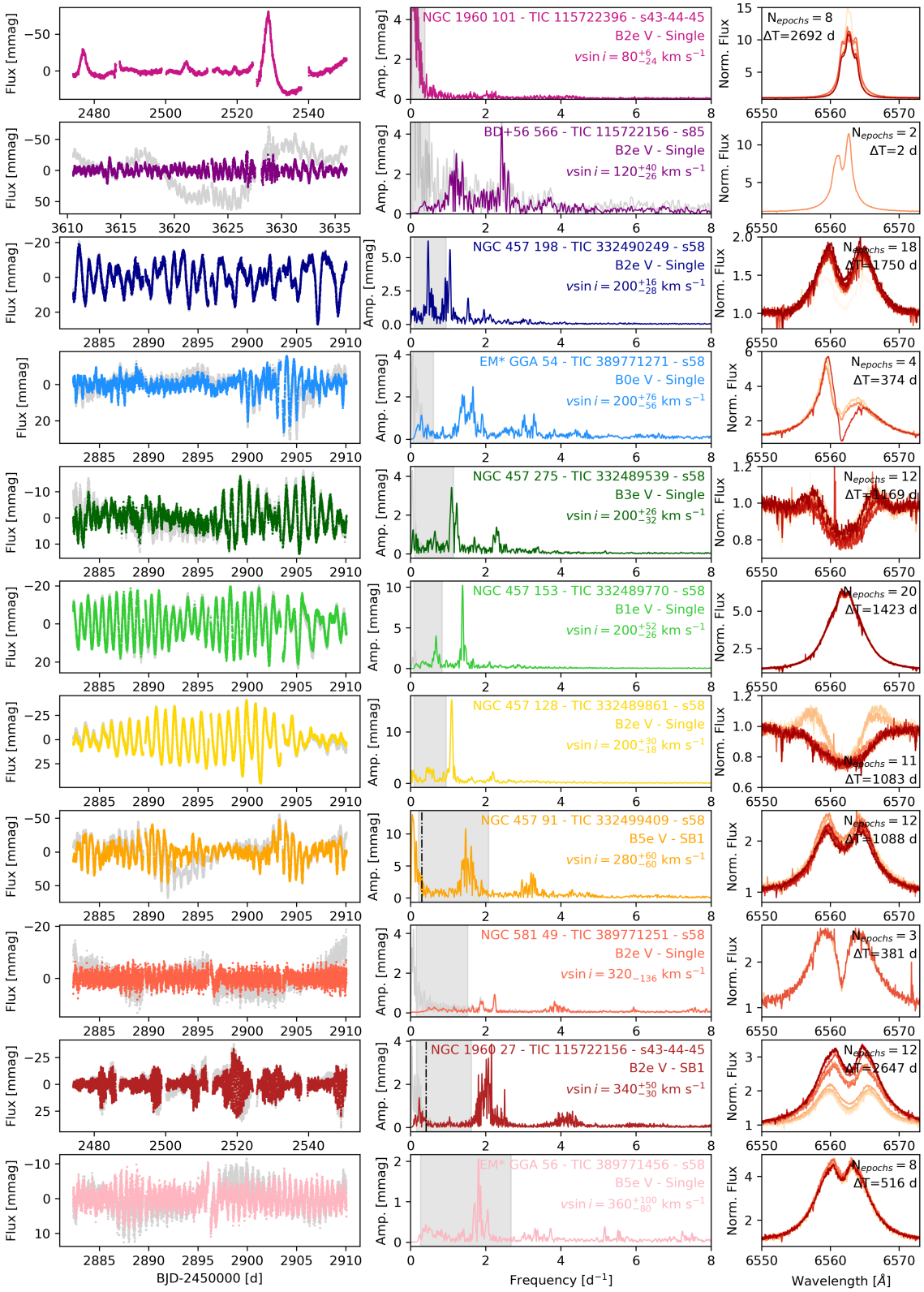

Figure 4. The light curves (left panels), frequency spectra (central panels), and the available HERMES spectra of Hα line (right panels) for the 11 non-contaminated pulsating Be stars across the four clusters. The stars are ordered top-to-bottom in increasing projected rotational velocity. In the left panels, we show both the non-detrended (light grey curve) and the detrended light curves (in colour), and the corresponding frequency spectra from these two light curves are shown in the middle panels in the same colour. The grey shaded regions in the frequency spectra represent the frequency range where rotational modulation may be expected given the measured v sin i and estimated radius of each star. The black vertical dash-dot lines in the middle panels show the orbital frequency for identified SB1 systems. In the right panels, we also report the number of spectroscopic epochs available and the total time coverage of the HERMES spectra (ΔT). The spectra are ordered from lighter (earliest epoch) to darker (latest epoch) colours. We note that the spectra are not contemporaneous with the TESS sectors.

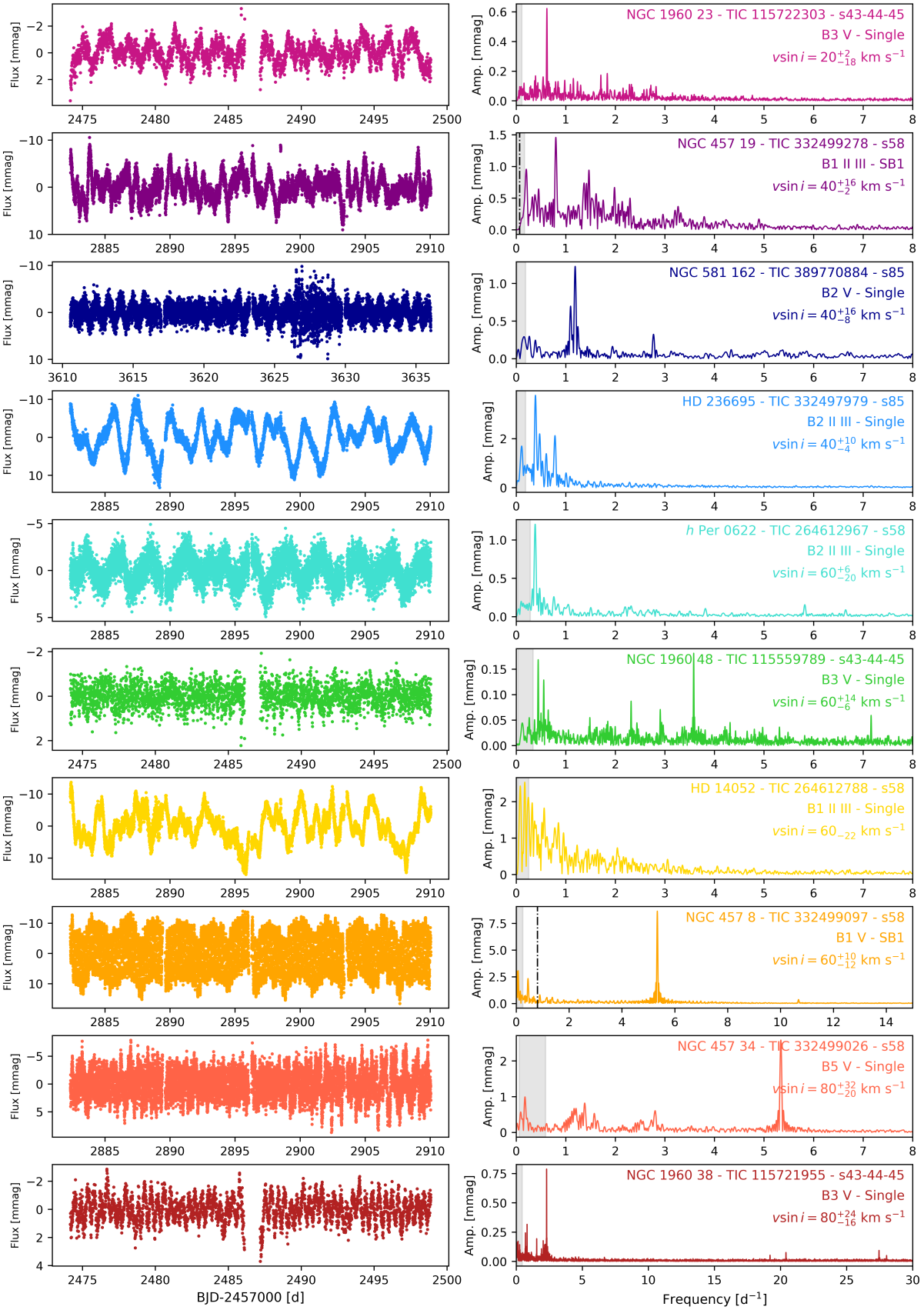

Figure 5. Light curves and frequency spectra for the slower rotating β Cep and hybrid stars that are not contaminated. The layout and styling are the same as Fig. 4, except the Hα panel is excluded since there are no emission features.

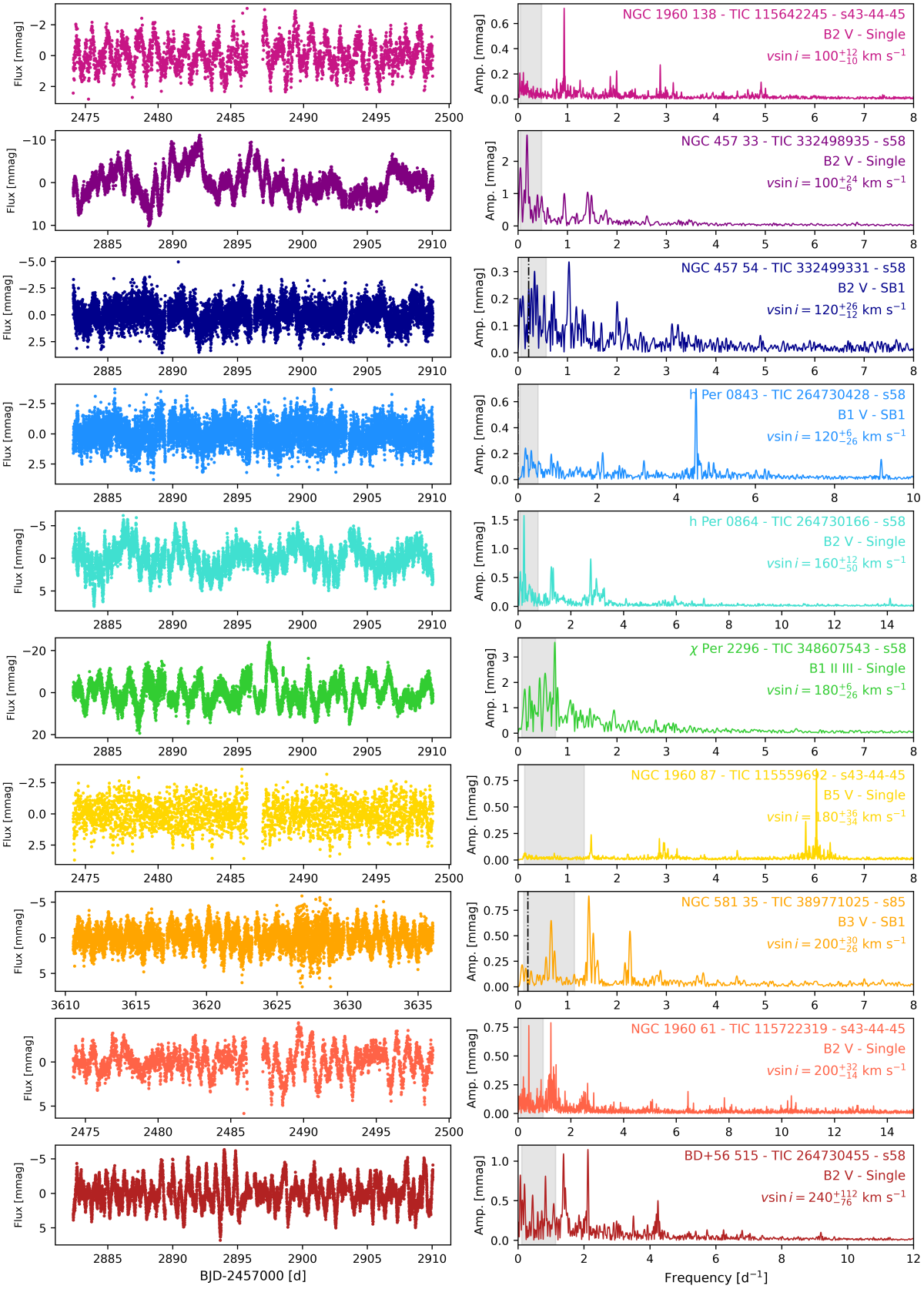

Figure 6. Same as Fig. 5 but for the β Cep and hybrid stars with $v\sin i \geq 100$ km s^{-1}.

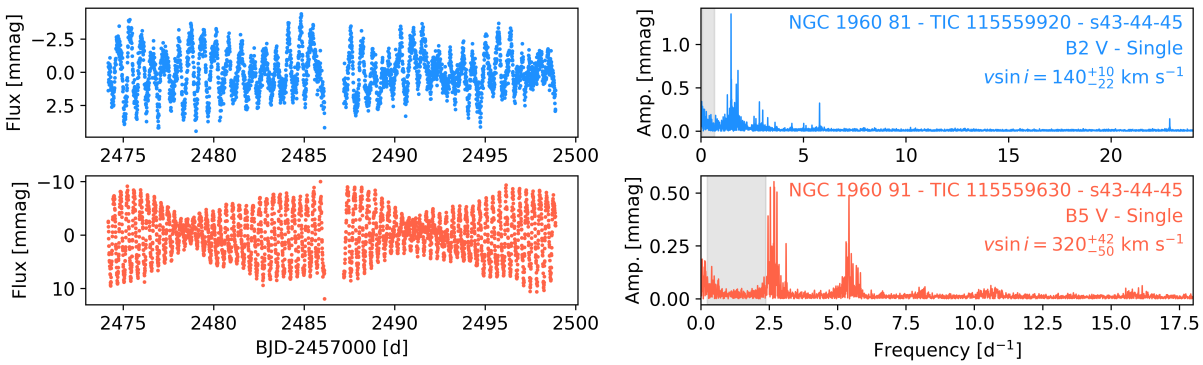

Figure 7. Same as Fig. 5 but for the SPB stars.

enables mode identification in terms of spherical harmonic geometry and facilitates forward asteroseismic modelling (e.g. Burssens et al. 2023; Vanlaer et al. 2025). For the fastest rotators (i.e. $v \sin i \geq 200$ km s^{-1}), frequency groups similar to those in pulsating Be stars are present. We have classified NGC 1960 91 as an SPB star, and it is the best example of this. It has a projected rotational velocity of 320 km s^{-1} and the TESS light curve shows complex beating patterns and frequency groups, as shown in Fig. 7, but it does not show any emission in the Hermes spectra. The dFT of the star shows groups of frequencies above 4 d^{-1}, but upon inspection, they appear to be harmonics of the group with higher amplitudes at ~ 2.5 d^{-1}. Thus, this star could either be considered a rapidly rotating SPB star and not a Be star, or a hybrid star, and is an example of how classifying pulsators without mode identification is not straightforward.

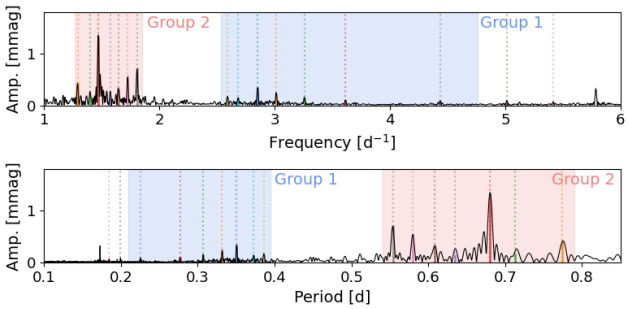

Figure 8. The frequency spectrum and periodogram of the TESS light curve of NGC 1960 81 are shown in the top and bottom panels, respectively. In each panel, the 18 significant gravity-mode frequencies are identified as vertical dotted lines with arbitrary but consistent colours across the two panels for ease of identification. The two shaded regions denote two distinct gravity-mode period-spacing patterns, denoted as group 1 in blue and group 2 in red.

4 ASTEROSEISMOLOGY OF NGC 1960 81

In this Section, we perform forward asteroseismic modelling of a pulsating cluster member, NGC 1960 81, to constrain its age. This allows us to independently verify the literature cluster age using asteroseismology and explore any differences.

The majority of stars in the sample have a high projected rotational velocity ($v \sin i > 100$ km s^{-1}), and so we do not expect to identify any symmetric rotationally split multiplets. Moreover, given that only one 27-d TESS sector is available for most stars, the poor resultant frequency resolution makes it challenging to robustly identify individual pulsation mode frequencies for most stars. Nonetheless, we visually inspected the frequency spectra and periodograms of all 33 isolated stars to search for potential (a)symmetric rotational splittings. As expected, this search was unsuccessful.

However, in this search five stars were identified as candidates for having gravity-mode period spacing patterns, with each of these stars having three consecutive sectors of TESS data: NGC 1960 27, NGC 1960 61, NGC 1960 81, NGC 1960 87 and NGC 1960 91. Scott & Bowman (2026) demonstrated that at least 3-6 months of consecutive TESS sectors are needed to reliably extract a gravity-mode period spacing pattern. Given that NGC 1960 81 has the largest number of independent pulsation modes detected, we focus on this target. Ultimately, it was possible to extract two period spacing patterns for NGC 1960 81. In the following sections, we discuss the methodology for the fitting process and the forward asteroseismic analysis that followed.

4.1 Detection of period spacing patterns

NGC 1960 81 (TIC 115559920; Gaia DR3 3449518106367398784) has a spectral type of B2 V and shows no signature of binarity from spectroscopy, with a projected rotational velocity of $v \sin i = 140^{+10}_{-22}$ km s^{-1}, an effective temperature of 18000 ± 400 K, and a surface gravity of $4.02^{+0.02}_{-0.15}$ dex derived from a grid of tlusty atmospheric models in Paper 1. As discussed in Section 2.5, these atmospheric parameters are generally consistent with those provided in the Gaia ESP-HS catalogue, which are $T_{\rm eff} = 18063 \pm 379$ K and $\log g = 4.02 \pm 0.06$.

In this work, we classify NGC 1960 81 as an SPB star based on its multi-periodic gravity-mode pulsations spanning $0.17 \leq f \leq 22.86$ d^{-1} in its TESS light curve. The frequency spectrum of the three consecutive TESS sectors 43, 44, and 45 and the corresponding periodogram are shown in Fig. 8. The frequency spectrum exhibits two distinct gravity-mode period spacing patterns, which are denoted as group 1 and group 2 in Fig. 8. The dominant frequency of each pattern is 2.86 d^{-1} and 1.47 d^{-1}, respectively. There are two additional isolated peaks at 5.78 d^{-1} and 22.86 d^{-1}. A total of 21 significant frequencies were initially extracted, of which two did not satisfy the Loumos–Deeming criterion for being resolved by $2.5/\Delta T$ from other frequencies (see Eq. 2). An analysis of combination and harmonic frequencies identified only the frequency of 5.78 d^{-1} to be a combination frequency of 3.01 d^{-1} and 3.26 d^{-1}, resulting in a final set of 18 significant frequencies.

To fit the observed gravity-mode period spacing patterns, the Python package AMIGO[6] (Asymptotic Modelling of Gravity-mode Oscillations; Van Reeth et al. 2016, 2018) was used. AMIGO computes the theoretical asymptotic gravity-mode period spacing (Π_0) for rotating stars and measures near-core rotation rates ($f_{\rm rot}$) by analysing their gravity-mode pulsations. Assuming that the star is uniformly rotating and spherically symmetric, neglecting the effects of the centrifugal force and that the gravity-mode pulsations are in the asymptotic regime allows the use of the Traditional Approximation of Rotation (TAR; Berthomieu et al. 1978; Mathis & Prat 2019). The TAR eigenvalues required for the computation modes were obtained from precomputed grids generated with GYRE (Townsend & Teitler 2013), which are used internally by AMIGO. An input of the AMIGO software is the mode geometry of a gravity-mode period-spacing pattern, as well as a list of periods, amplitudes, phases and their corresponding uncertainties. The approach of AMIGO allows for missing mode periods, thus it can handle gaps in a period-spacing pattern, which is particularly advantageous when limited frequency resolution hampers the identification of all significant peaks.

Table B3 lists the gravity-mode periods we identified as members of period-spacing patterns for NGC 1960 81 and included in the AMIGO fitting process. Initially, the two groups of gravity modes were analysed separately before the final combined fit, which we discuss in the next subsections. The results of the AMIGO fitting are reported in Table 2. The AMIGO fits and the χ^2 distribution plots for $f_{\rm rot}$ and Π_0 are shown in Figs. B1, B2 and B3.

4.1.1 Group 1: a prograde dipole pattern

In Fig. 8, group 1 denotes the higher-frequency gravity-mode period spacing pattern of NGC 1960 81, and has a dominant peak at 0.35 d (2.85 $\rm d^{-1}$). In total, seven significant periods were identified and included in the AMIGO fit, along with two necessary gaps to create an unbroken period-spacing pattern, which are provided in Table 2. The gravity-mode period spacing pattern of group 1 shows a clear negative gradient, which is indicative of a series of consecutive radial order prograde modes (see Bouabid et al. 2013). We used AMIGO with different combinations of mode geometries to determine the best-fitting model. We found that different mode geometries showed reasonable solutions in terms of reduced χ^2 values. Ultimately, the period spacing pattern of group 1 was identified as a prograde dipole mode pattern, and the evidence for this as the best-fitting mode geometry is four-fold. First, the fit had the lowest reduced χ^2 value of all the attempted geometries. Second, prograde dipole modes are the most common form of period spacing patterns found in early-type dwarfs (see Van Reeth et al. 2016; Li et al. 2020; Szewczuk et al. 2021; Pedersen et al. 2021; Fritzewski et al. 2026). Third, gravity modes with increasing values of angular degree and varying azimuthal degree beyond $\ell = 1$ provided unphysical values of Π_0 (e.g., $\ell = 2$, $m = 1$ yielded $\Pi_0 = 27000$ s, and increasing to 43000 s for $\ell = 4$, $m = 1$), which is unlikely for NGC 1960 81 given its spectral type and atmospheric parameters. For example, $\Pi_0 \gtrsim 25000$ s suggests a mass above 10 $\rm M_\odot$ (Johnston et al. 2019a; Scott & Bowman 2026), which is discrepant with the evolutionary mass of NGC 1960 81 given its location in the HR diagram (see Fig. 3). Finally, geometric cancellation makes it far less likely to observe higher angular degrees (Dziembowski 1977).

Establishing a prograde dipole geometry for the group 1 period spacing pattern, the best-fitting near-core rotation frequency is $f_{\rm rot,\,group1} = 1.88 \pm 0.07$ $\rm d^{-1}$ and the asymptotic period spacing is $\Pi_{0,\,\rm group1} = 13000 \pm 1567$ s according to the best-fit with AMIGO. The χ^2 distributions and the fit to the period-spacing pattern for group 1 by AMIGO are shown in Fig. B1.

Assuming rigid rotation and using the radius obtained from the forward modelling ($R = 3.89$ $\rm R_\odot$), we use Eqn. (1) to estimate the inclination from the spectroscopic value of $v \sin i = 140^{+10}_{-22}$ $\rm km\,s^{-1}$. For the prograde dipole gravity-mode period spacing pattern of group 1, we calculate $\rm v_{rot} = 366 \pm 14$ $\rm km\,s^{-1}$, thus an inclination of 23^{-2}_{+4} degrees. The uncertainties associated with $\rm v_{rot}$ and the inclination were calculated using standard error propagation.

4.1.2 Group 2: a potential retrograde pattern

The period spacing of group 2 contains a dominant period of 0.68 d (1.47 $\rm d^{-1}$; see Fig. 8). Six additional significant frequencies comprise this period-spacing pattern as well as two gaps (see Table B3). The gradient of this period spacing pattern is negative, which indicates it comprises retrograde modes (see Bouabid et al. 2013). These are fairly uncommon in early-type dwarfs, but more often seen in rapid rotators (see Van Reeth et al. 2016, 2018; Li et al. 2020). As for group 1, we fitted different mode geometries using AMIGO, ranging from $\ell = 2$ $m = -2$ to $\ell = 5$ $m = -1$ (the last available file in the GYRE grid). The mode geometry $\ell = 1$ $m = -1$ was also tested, but it did not fit the pattern, so it was excluded immediately. All tested mode geometries provided comparably good fits in terms of their reduced χ^2 values. The inferred values of Π_0 and $f_{\rm rot}$, however, differed substantially. For lower angular degrees, the asymptotic period spacing was between 300 and 900 s, which is very low for main-sequence stars with masses between 3 and 10 $\rm M_\odot$ (Johnston et al. 2019a; Scott & Bowman 2026). For $3 \leq \ell \leq 5$, Π_0 increases with increasing ℓ, but so did the near-core rotation frequency (e.g. $\ell = 5$, $m = -1$ yielded $\Pi_{0,\,\rm group2} = 5400 \pm 633$ s and $f_{\rm rot,\,group2} = 4.73 \pm 0.50$ $\rm d^{-1}$).

In the absence of other information, the only concrete conclusion that can be made is that the period-spacing pattern of group 2 is retrograde. The only mode geometry for group 2 that provides a similar value of Π_0 and $f_{\rm rot}$ to the group 1 solution is $\ell = 5$, $m = -1$, which yields $\Pi_{0,\,\rm group2} = 5400 \pm 633$ s and $f_{\rm rot,\,group2} = 4.73 \pm 0.50$ $\rm d^{-1}$. The mostly flat χ^2 distributions and the AMIGO fit to the period-spacing pattern for group 2 are shown in Fig. B2. We stress that this solution for group 2 should not be interpreted as a robust solution. For example, the implied near-core rotation from group 2 corresponds to a surface velocity of $\rm v_{rot} = 965 \pm 102$ $\rm km\,s^{-1}$, which exceeds the critical rotation of an early-B star (Townsend et al. 2004).

4.1.3 Combined fit

Finally, we fitted the two gravity-mode period spacing patterns of group 1 and group 2 simultaneously using AMIGO, adopting the mode geometries of $\ell = 1$, $m = 1$ and $\ell = 5$, $m = -1$ that were favoured by the individual fits. This yielded $\Pi_{0,\,\rm combined} = 13800 \pm 300$ s and $f_{\rm rot,\,combined} = 1.92 \pm 0.02$ $\rm d^{-1}$. The fit to the period-spacing pattern for the combined fit of group 1 and group 2 using AMIGO is shown in Fig. B3, as well as the χ^2 distributions. We emphasise that whilst the combined fit provides smaller confidence intervals for both Π_0 and $f_{\rm rot}$ compared to the AMIGO fit of group 1, the uncertainty in the mode geometry identification of group 2 may be misleading. On the other hand, since the combined solution agrees with group 1 in terms of Π_0 and $f_{\rm rot}$, this may validate the mode geometry identification of group 2.

Regardless, the combined fit demonstrates that the probing power

[6] https://github.com/TVanReeth/amigo

Table 2. Asteroseismic results of gravity-mode period spacing patterns in NGC 1960 81. The first and second columns report the setup and the mode geometries, columns 3-5 report the asymptotic period spacing, the near-core rotation frequency, and the reduced χ^2 from the AMIGO fitting process. Columns 6-11 report the results from forward asteroseismic modelling.

	Mode geometry	Π_0 [s]	$f_{\rm rot}$ [d^{-1}]	$\chi^2_{\rm red}$	$T_{\rm eff}$ [K]	log g	Age [Myr]	M [M$_\odot$]	R [R$_\odot$]	$f_{\rm CBM}$
Group 1	$\ell = 1, m = 1$	13000 ± 1567	1.88 ± 0.07	185	18197	4.02	51.2	5.75	3.89	0.040
Group 2	$\ell = 5, m = -1$	5400 ± 633	4.73 ± 0.50	713	16982	3.78	65.7	5.75	4.08	0.005
Combined	$\ell = 1, m = 1$ and $\ell = 5, m = -1$	13800 ± 300	1.92 ± 0.02	414	18197	3.99	48.4	6.00	5.12	0.040

of gravity-mode asteroseismology for NGC 1960 81 is dominated by the period spacing pattern of group 1. This is related to the fact that the detection and analysis of a prograde dipole pattern is typically more reliable than that of higher angular degree modes. Again, using the radius determined from the asteroseismic forward modelling of the likely retrograde pattern alone ($R = 5.12\,R_\odot$) and rigid rotation, the fit of the combined period-spacing patterns yields $v_{\rm rot} = 492 \pm 5$ km s^{-1} and an inclination of 17^{-1}_{+3} degrees, with uncertainties determined through error propagation.

4.2 Forward asteroseismic modelling

The forward asteroseismic modelling was performed using a grid of MESA models (r10108; Paxton et al. 2011, 2013, 2015, 2018) pre-computed by Johnston et al. (2019a). This grid spans a wide range of stellar masses (1.2–25 M$_\odot$ in varying step sizes) and different values of diffusive exponential convective boundary mixing (CBM; $f_{\rm CBM}$, from 0.005 to 0.040 in steps of 0.005). An envelope mixing term, log $D_{\rm env}$, is included but kept constant, to represent the mixing at the base of the envelope, effectively acting as a catch-all parameter for extra mixing processes. In this work, log $D_{\rm env}$ is fixed to log $D_{\rm env}$ = 1 cm^2 s^{-1}, following Burssens et al. (2020). This is because forward asteroseismic modelling of gravity modes based on only Π_0 is not so sensitive to envelope mixing (Johnston et al. 2019a). Instead, Π_0 is particularly sensitive to the convective core mass, and hence the bulk properties of a star such as mass and age (see Miglio et al. 2008).

We follow the same approach as Johnston et al. (2019b) and Scott & Bowman (2026) and use a maximum likelihood statistical framework with the Mahalanobis distance (MD) as a merit function to fit Π_0 as our asteroseismic observable alongside the spectroscopic constraints of $T_{\rm eff}$ and log g, which is a methodology originally described by Aerts et al. (2018). A likelihood for each model in the grid is calculated using the MD merit function, and the 36th and 68th percentiles of the normalised probability for the distribution of all models are used to estimate 1σ confidence intervals for each marginalised free parameter. Of the three observables to be fitted with the grid, Π_0 is obtained from our AMIGO analysis, and $T_{\rm eff}$ and log g are taken from the spectroscopic analysis.

We tested if either of Gaia ESP-HS parameters or those from the TLUSTY grid-based analysis of Paper 1 made a difference, and it did not change the results of the forward asteroseismic modelling because they are consistent with each other. This demonstrates that the modelling result is largely dominated by the value and confidence interval of Π_0 for NGC 1960 81. However, it is not wise to remove $T_{\rm eff}$ and log g as observables, because Π_0 is a highly degenerate parameter within the large grid. Therefore, $T_{\rm eff}$ and log g are needed to delimit the parameter space. Ultimately, we opt to use the Gaia ESP-HS parameters since they have smaller uncertainties.

With this setup, we performed forward asteroseismic modelling using the same values of $T_{\rm eff}$ and log g but with three different values of Π_0, which were the outputs of our AMIGO analysis of the period spacing patterns of group 1, group 2, and the combined fit. The resultant best-fitting values for the age, mass, CBM, as well as the inferred $T_{\rm eff}$, and log g are reported in Table 2. We discuss the individual results of each of the three scenarios in the following subsections.

4.2.1 *Group 1*

The results of the forward asteroseismic modelling of the prograde dipole gravity-mode period spacing pattern in group 1 are in the first row of Table 2. The inferred $T_{\rm eff}$ and log g are consistent with the values obtained from the TLUSTY analysis and from the Gaia ESP-HS catalogue. The inferred stellar mass of 5.75 M$_\odot$ is somewhat lower than the mass inferred from the spectral type, which is around 7.30 for a B2 V (Pecaut & Mamajek 2013). For this solution, the best-fitting value for the diffusive exponential CBM parameter is the highest value available in the grid, $f_{\rm CBM} = 0.04$, and the corresponding age of 51 Myr is 21 Myr larger than the isochrone age of 30 Myr reported by Dias et al. (2021). We show the histograms showing the number of models within 1σ limit for the group 1 solution in Fig. 9.

Overall, this is a reasonable fit given the limitations imposed by the short TESS light curves. This also demonstrates that a relatively consistent age from forward asteroseismic modelling can be obtained for a pulsating massive star in an open cluster with only a few months of space photometry.

4.2.2 *Group 2*

We also performed forward asteroseismic modelling using only the group 2 period-spacing pattern. The best-fitting parameters are listed in the second row of Table 2. Compared to the group 1 solution, the inferred $T_{\rm eff}$ and log g are slightly lower, while the inferred mass is consistent. The largest differences are in the amount of CBM and age; the preferred values are $f_{\rm CBM} = 0.005$ and the inferred age is about 15 Myr larger than for Group 1. Whilst the forward asteroseismic modelling solution is not completely consistent with that of group 1, it is not too different. This lends support that the retrograde period-spacing pattern of group 2 could indeed have quite a high angular degree, since lower values of ℓ for group 2 provide much worse asteroseismic solutions.

4.2.3 *Combined solution*

Lastly, we performed forward asteroseismic modelling using Π_0 = 13800 ± 300 s that we obtained from the AMIGO fit of both period-spacing patterns from group 1 and group 2. The resultant parameters are shown in the last row of Table 2. Compared to the solution from modelling only group 1, the combined fit yields a slightly smaller age, while still having the highest amount of CBM. Overall, we conclude

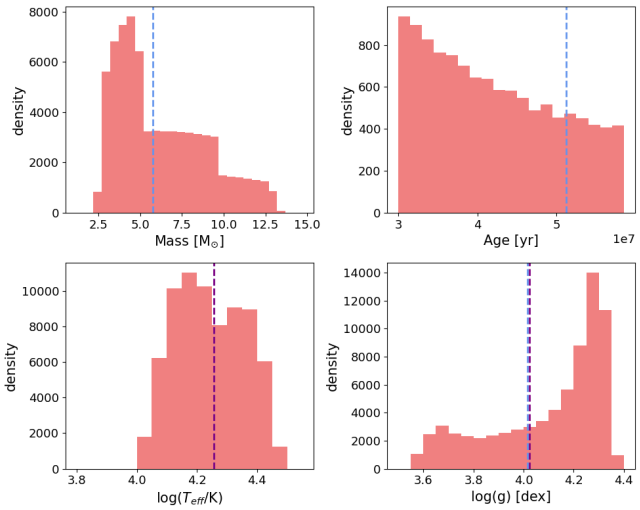

Figure 9. Histograms showing the number of models within 1σ limit for the forward asteroseismic modelling of the group 1 period spacing pattern. In order from top left, there are mass, age, effective temperature and surface gravity. The dashed blue vertical lines are the best-fit parameters. For $T_{\rm eff}$ and $\log g$, the input Gaia parameters are also shown with a purple vertical line.

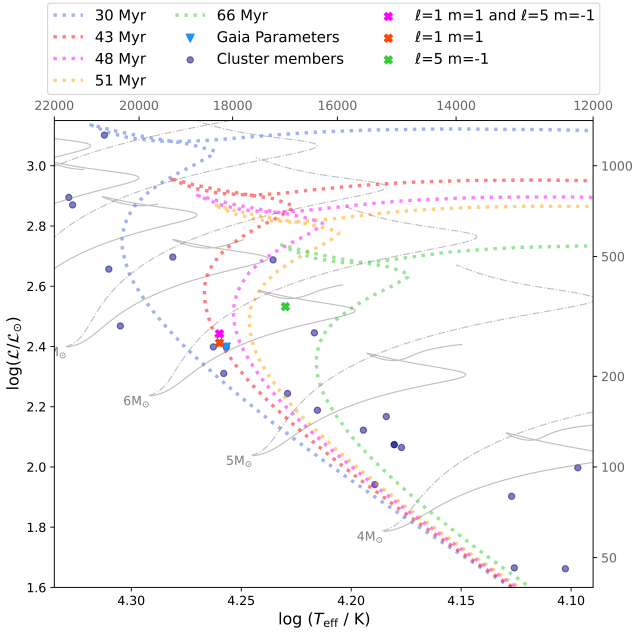

Figure 10. Spectroscopic HR diagram of the cluster NGC 1960, with the cluster members shown as blue points. The three outcomes of forward asteroseismic modelling of NGC 1960 81 are shown as coloured crosses in the legend. The Gaia parameters of NGC 1960 81 are represented with a blue triangle. Four PARSEC (Bressan et al. 2012) isochrones of different ages are shown with their ages reported in the legend. The stellar evolutionary tracks shown as solid lines for $f_{\rm CBM} = 0.005$ and dashed lines for $f_{\rm CBM} = 0.04$ are from Johnston et al. (2019a).

that the solutions for only group 1 and the combined fit are consistent with each other. Hence, for simplicity, the impact of the ambiguous mode geometry identification of group 2 does not appear to play a major role in determining the overall best-fitting solution.

4.3 Interpretation of results and comparison of ages

Our analysis demonstrates that the identification of group 1 as a prograde dipole gravity-mode period spacing pattern is robust. Nevertheless, including group 2 in our modelling reduces the overall uncertainties of the combined AMIGO fit and yields forward asteroseismic modelling results that are more consistent with spectroscopy.

If the mode geometry identification of group 2 as $\ell = 5$, $m = -1$ is correct, then this may be explained by rapid rotation. Given that NGC 1960 81 is a rapid rotator (i.e. $v \sin i = 140^{+22}_{-10}$ km s^{-1} and inferred $v_{\rm rot} = 946 \pm 102$ km s^{-1}, due to the higher near-core rotational frequency), it is highly likely oblate. In this scenario, gravity darkening decreases the effective temperature and surface gravity of the equator, which unless the star is viewed pole-on, would make it appear cooler and older. The high-ℓ pulsations of rapid rotators (see Aerts et al. 2010) tend to have surface amplitudes that are maximal in equatorial bands. Moreover, fast rotators in clusters have been shown theoretically to appear older than more slowly rotating counterparts (Wang et al. 2020, 2023). This interpretation for NGC 1960 81 is supported by its position in the HR diagram (Fig. 10). For example, the forward asteroseismic modelling of only the retrograde group 2 period-spacing pattern yielded an age of $\sim$ 66 Myr, whereas the prograde dipole group 1 period-spacing pattern yields $\sim$ 51 Myr. This age discrepancy can be accounted for by the star's rapid rotation, especially given the reported cluster age of 30 Myr (Dias et al. 2021).

It is expected, and found again in our study, that the inferred age of an early-type dwarf star (i.e. a star with a convective core on during the main sequence) depends strongly on the amount of CBM, which is parametrised in our grid of 1D stellar evolution models as $f_{\rm CBM}$. If instead of treating $f_{\rm CBM}$ as a free parameter, and performing several independent fits with different values, the inferred age of NGC 1960 81 increases from $\sim$ 37 Myr for $f_{\rm CBM} = 0.01$ to $\sim$ 51 Myr for $f_{\rm CBM} = 0.04$. This is direct evidence that larger CBM prolongs the main-sequence lifetime, thus allowing the star to remain hotter than expected before reaching the spectroscopic value of $T_{\rm eff}$. The location of NGC 1960 81 and its best-fitting asteroseismic solutions are shown in the HR diagram in Fig. 10, as well as PARSEC (PAdova TRieste Stellar Evolution Code Bressan et al. 2012; Chen et al. 2015) isochrones of different ages. Johnston et al. (2019b) demonstrated that a range of potential $f_{\rm CBM}$ values for early-type dwarfs gives rise to isochrone-clouds, since different amounts of CBM can mimic an isochrone of a different age. Given this spread, the best-fitting asteroseismic age of 43 Myr is in reasonable agreement with the PARSEC isochrone age of 30 Myr, which uses only a single value of CBM in the underlying evolutionary models.

To investigate this further, we also compared the asteroseismic solutions for various fixed values of $f_{\rm CBM}$ to the PARSEC isochrone age of 30 Myr. The PARSEC isochrones adopt a step function for CBM with $\alpha_{\rm CBM} = 0.25$, which roughly corresponds to $f_{\rm CBM} = 0.025$ when using the diffusive exponential prescription for CBM (Moravveji et al. 2015, 2016). The asteroseismic age with a fixed value of $f_{\rm CBM}$ is 42 Myr, which is similar. However, we emphasise that the underlying physics and numerical prescriptions between PARSEC and our MESA models are quite different, so it is encouraging that the ages are so similar from two independent methods.

Moreover, we determined ages for all cluster members of NGC 1960 with BONNSAI[7] (Schneider et al. 2014), which employs a Bayesian method that compares all available observables to stellar

[7] https://www.astro.uni-bonn.de/stars/bonnsai/

structure and evolution models calculated using the Bonn evolutionary tracks (Brott et al. 2011), while accounting for observational uncertainties and prior information (e.g. the initial mass function and the distribution of rotational velocities). Like PARSEC, BONNSAI uses a grid of evolution models with a step function for CBM with $\alpha_{\rm CBM} = 0.035$. For NGC 1960 81, BONNSAI yields an age of $33.69^{+4.74}_{-6.1}$ Myr, which is consistent with the PARSEC cluster isochrone age ($\sim$ 30 Myr). For the other stars with available $T_{\rm eff}$ and $\log g$, BONNSAI ages fall between 25 and 50 Myr for most of the sample. This supports the reliability of the isochrone age, but also demonstrates that a spread of ages is expected because of different amounts and/or implementations of CBM in different evolution codes.

Although fully consistent with each other, the PARSEC isochrone and BONNSAI ages are somewhat smaller than the asteroseismic age for NGC 1960 81 of 43 Myr. However, this discrepancy is only at the 2σ level. The PARSEC isochrones are based on non-rotating evolutionary tracks with a lower level of mixing, which shortens the main-sequence lifetime and yields a younger cluster age. The discrepancy between BONNSAI and the asteroseismic age may reflect differences in the prescriptions for CBM and rotational mixing, or their numerical implementation, which we deem to be the most likely explanation. On the other hand, if the asteroseismic age is to be trusted compared to the others, this rapidly rotating star may have undergone a binary interaction that affected its surface and internal properties. While this is difficult to evidence in the analysis, since Π_0 is a diagnostic of the core mass and age of a star, any difference in asteroseismic age based on the core properties compared to the age inferred from the surface properties (e.g. PARSEC and BONNSAI) may be a result of binary interaction. Wang et al. (2020, 2023) argued using population synthesis models that there is a bimodal distribution of rotation rates that likely causes a split main-sequence in young open clusters (up to 40 Myr old). They showed that the different rotation rates can cause an age spread up to 20 Myr, more specifically up to 0.58 times the age of the cluster for a cluster with a turn-off mass of 8 $M_\odot$ (Wang et al. 2020). If we assume that the PARSEC age of NGC 1960 of 30 Myr old is correct, then the difference in the asteroseismic age of the star NGC 1960 81 could be explained by the fast rotation of the star.

5 REVISITING BINARY SYSTEMS WITH TESS LIGHT CURVES

In Paper 1, RV variability from multi-epoch HERMES spectroscopy was used to identify spectroscopic binaries across the four young open clusters studied in this work. To investigate the possible degeneracies between pulsations and binarity when identifying spectroscopic RV variability, we compare the photometric period ($P_{\rm phot}$) identified in this work with the spectroscopic period ($P_{\rm spec}$) determined in Paper 1. We note that the eight additional stars in this work that were added to the sample of 74 stars from Paper 1 were previously excluded because either their spectral types were later than B5, or only one or two spectra were available, preventing an RV analysis. This means that these eight stars do not yet have any evidence for binarity.

In Fig. 11, we compare the dominant photometric period from our analysis of TESS light curves to the inferred spectroscopic binary period for the subset of 23 candidate binary systems. The remaining five stars that are not included in Fig. 11 either have too high contamination or did not show any significant photometric variability in their light curve. If the spectroscopic period is consistent with the photometric one, all photometric binaries (i.e. EBs, ellipsoidal variables) and stars with rotational modulation should lie on the bisector. Only one of these is an anomaly, EM* GGA 52, which is an EB with a photometric period that is twice the reported spectroscopic period from Paper 1. Therefore, the previously reported binary period of $P_{\rm spec} = 2.2507 \pm 0.0002$ d is likely an alias of the true binary period of $P_{\rm phot} = 4.502164 \pm 0.000003$ d.

All other stars in Fig. 11 that do not lie on the bisector have $P_{\rm phot}$ that significantly differs from their reported $P_{\rm spec}$. All such systems are pulsators (i.e. β Cep, hybrid, or Be). Thus, it is likely that the binary period inferred from the spectroscopic RV analysis is correct, and that the dominant photometric period is due to pulsations.

Closer inspection of the Be stars in Fig. 11 shows small values for both $P_{\rm spec}$ and $P_{\rm phot}$. As mentioned in Section 3.1, it was not possible to extract the light curves of all Be stars in our sample due to contamination. Of the four Be stars in binaries reported by Paper 1, only two did not show a high level of contamination, NGC 457 91 and NGC 1960 27, which are shown in Fig. 11. With constraints on the pulsation periods for both stars now known from the TESS light curves, it becomes clear that the previously identified value of $P_{\rm spec}$ is likely a pulsation period and not a binary period. Moreover, the orbital solutions reported by Paper 1 for the two purported Be-star binary systems were not robust (see appendix of Paper 1), and the RV variability was also quite high (i.e. $\Delta RV = 41 \pm 8$ km s^{-1} for NGC 457 91 and $\Delta RV = 29 \pm 8$ km s^{-1} for NGC 1960 27). With our new analysis of TESS light curves and the complementary HERMES spectroscopy, we conclude that these two Be stars are apparently single stars, with RV variability caused solely by pulsations. This suggests that the 20 km s^{-1} threshold commonly used for distinguishing binarity from pulsations (Banyard et al. 2022; Bodensteiner et al. 2025; Villaseñor et al. 2025) may need to be larger for Be stars. The binary status of the other two Be stars that were also classified as binaries but with small values of $P_{\rm spec}$ should also be questioned, but since it was we could not extract the TESS light curves, it is not possible to make a final statement if the determined orbital period is actually their pulsation period.

If these Be stars in short-period binaries are reclassified as single stars, we can re-calculate the observed binary fraction of the two clusters as 53 ± 11 per cent for NGC 457, and 27 ± 11 percent for NGC 1960. Note that these values are computed based on the sample of 18 stars analysed in Paper 1, thus the five later type stars are similarly excluded for consistency reasons. These observed binary fractions are 5 and 3 per cent lower, respectively, compared to those derived in Paper 1. Using the same methodology as Paper 1, the bias-corrected intrinsic binary fractions are reduced by 8 and 13 per cent, respectively, and are 75^{-26}_{+28} per cent for NGC 457 and 68^{-43}_{+32} for NGC 1960. Although slightly lower, these intrinsic binary fractions are still consistent with each other within their 1σ confidence intervals, and the other two clusters studied in this work. Therefore, the conclusion of Paper 1 is still valid that the majority of early B-type stars in galactic clusters of ages between 15 and 30 Myr are in binaries.

In the following sections, we discuss all photometric binaries and stars with rotational modulation that arose from our analysis of the TESS light curves. Binary modelling of the TESS light curves is beyond the scope of this paper, but it is the subject of future work. All the identified EBs were previously known in the literature, while the one ellipsoidal variable (NGC 1960 134) and the systems that show rotational modulation (NGC 1960 8, NGC 1960 16 and χ Per 2185) were previously unknown as such.

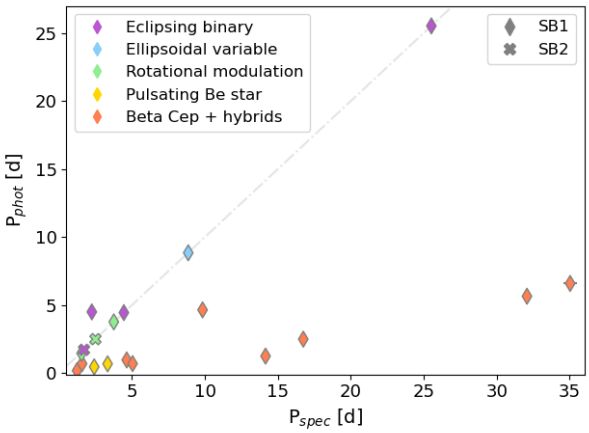

Figure 11. Dominant photometric period from TESS light curves versus spectroscopic period from RV analysis for binaries reported in Paper 1. Symbol colours denote the different classes of pulsators, and different symbol styles denote the type of binaries (SB1 or SB2). The dashed grey line is the bisector.

5.1 Photometric binaries

We identify five photometric binaries in our sample. Their TESS light curves, phase-folded light curves, and frequency spectra are shown in Fig. 12. Four of these are EBs, χ Per 2311, NGC 457 37, NGC 457 85, and EM* GGA 52, and one is an ellipsoidal variable: NGC 1960 134. The four EBs were all previously known, but the ellipsoidal variable is a newly detected system. The five systems were also identified as spectroscopic binaries in Paper 1, where the orbital solution was also determined and consistent with the photometric period except for EM* GGA 52 as mentioned previously, in which the spectroscopic period was an alias of the true photometric binary period of ~ 4.5 d.

5.2 Rotational modulation

Finally, we discuss stars that show rotational modulation in their TESS light curves, which is commonly associated with the presence of chemical spots on their surfaces. The three stars with TESS light curves dominated by rotational modulation are NGC 1960 8, NGC 1960 16, and χ Per 2185. Their light curves, frequency spectra and spectroscopic variability of the He I λ5875 line are shown in Fig. 13. We discuss the three stars in the Appendix Sect.A3.

6 CONCLUSIONS

In this follow-up project, we carried out a photometric characterisation of 82 B-type stars in four young Galactic open clusters with ages between 15 and 30 Myr. Using data from the NASA mission TESS, we pushed the limits of photometric analysis in crowded cluster fields by applying a range of state-of-the-art light-curve extraction techniques. This allowed us to obtain reliable light curves for 63 stars and to tentatively classify the variability of 80 per cent of the full sample. Among the stars with usable light curves, nearly all exhibit variability consistent with pulsations, demonstrating that pulsational variability is ubiquitous among B-type stars.

Excluding two stars that showed no detectable variability, we divided the remaining 61 objects into three main categories: pulsating Be stars, classical pulsators (including β Cep stars, slowly pulsating B stars, and hybrids), and photometric binaries (including eclipsing binaries, ellipsoidal variables, and stars showing rotational modulation).

All Be stars in the sample show pulsational variability, confirming the results of previous surveys. Their frequency spectra are dominated by signals in the gravity-mode regime (below 4 d^{-1}), and all exhibit the characteristic frequency groups commonly observed in this class of stars.

β Cep stars constitute the most common class of pulsators in the sample, which is expected given that B2 dwarfs dominate the sample. Low-radial order pressure modes are also detected in stars of later spectral type, suggesting that the β Cep instability strip may extend to lower masses than predicted by classical instability strips. Very rapidly rotating stars ($v \sin i \geq 200$ km s^{-1}) show frequency groups caused by complex beating patterns in their light curves, similar to those observed in pulsating Be stars. Correctly identifying SPBs was challenging because most of the pulsators exhibit significant peaks above 4 d^{-1}, which is the typical threshold used to identify this class of pulsators. However, we identify five stars all in the cluster NGC 1960 as candidates for having period-space patterns, a typical characteristic of SPB stars.

For one of these stars, NGC 1960 81, it was possible to extract two period spacing patterns and then perform an asteroseismic forward modelling. The two extracted patterns are a prograde dipole and a retrograde pattern with high angular degree and low azimuthal degree ($\ell = 5$, $m = -1$). The two patterns were fitted individually and then combined, and the same thing was done regarding the forward modelling. The prograde dipole solution yields stellar parameters consistent with the spectroscopic results, whereas the retrograde solution alone gives significantly different results and cannot be used independently to constrain the star. However, when combined with the prograde pattern, it provides tighter constraints on the stellar parameters. This suggests that the retrograde pattern probes the equatorial regions of the star, which are expected to be oblate as a result of rapid rotation. We compare the age of NGC 1960 81 with the isochrone age of the cluster and with the age determined using the Bayesian tool BONNSAI. We found that the asteroseismic age differs from the isochrone age and from the BONNSAI by about 15 million years. This difference might be due to the different models used in the three ages determination, or maybe the star went through some form of binary interaction process (e.g. mass transfer or merger).

Finally, we looked at the photometric binaries. Out of the 30 spectroscopic binaries identified in Paper 1, eight of them were also identified as photometric binaries. These include four eclipsing binaries, one ellipsoidal variable and three stars that showed rotational modulation. The four EBs were all previously known in the literature, while the ellipsoidal variable and the rotational modulation are newly identified. Two of the stars that show rotational modulation show undeniable signs of binarity in their spectra, with one of the two being an SB2 and the other having a radial velocity shift higher than 40 km s^{-1}, which is unlikely to be caused by pulsations. The third star does not show a clear radial velocity shift in the spectra due to low S/N, there could be a bias in the binary detection. No new binaries were identified through photometry, and three systems (the afore-mentioned rotational modulation star and two Be stars) might be incorrectly classified as binaries. Thus suggesting that, especially for pulsating Be stars, the 20 km s^{-1} used to identify binaries might be revisited.

Overall, this work highlights the importance of multifaceted characterisation for massive stars, considering that both binarity and pulsations are almost ubiquitous, and they influence each other. Lastly, we show the power of the TESS mission and what is possible to do in crowded fields and with only limited sectors.

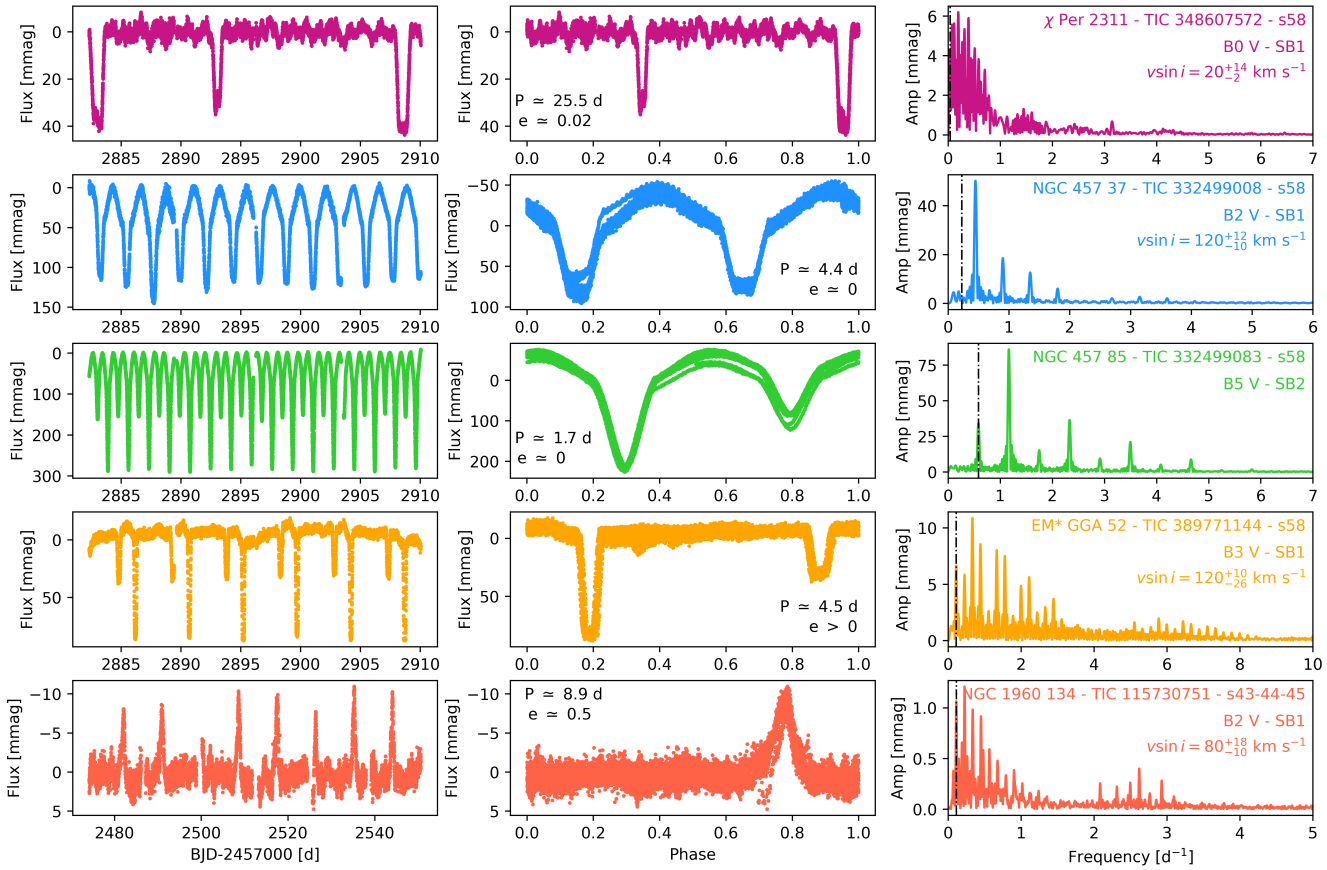

Figure 12. TESS light curves (left panels), phase-folded light curves (central panels), and frequency spectra (right panels) of the five photometric binaries from this work. The vertical dashed black lines in the right panels denote the orbital frequencies determined from spectroscopy in Paper 1.

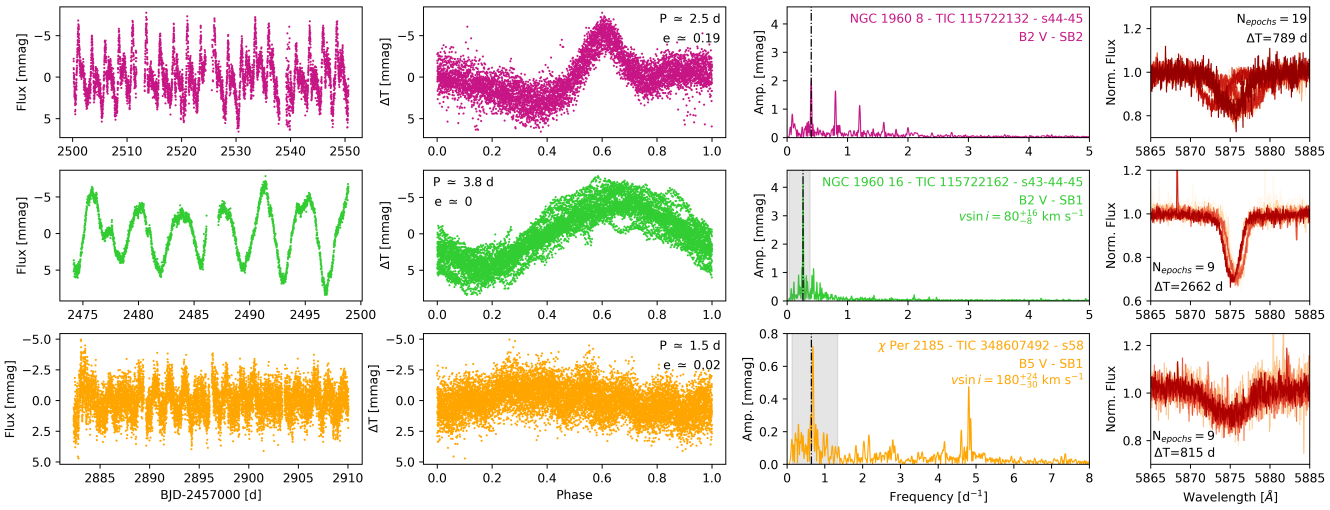

Figure 13. From left to right, the panels show the TESS light curves, the phase-folded light curves, and the frequency spectra of the three stars dominated by rotational modulation. The vertical dashed black lines in the right panels denote the purported orbital frequencies determined from spectroscopy in Paper 1, but here are demonstrated to be rotational modulation rather than binarity. In the right-most panel, the profile of He I from multi-epoch HERMES spectra is shown.

ACKNOWLEDGEMENTS

The authors gratefully acknowledge UK Research and Innovation (UKRI) in the form of a Frontier Research grant under the UK government's ERC Horizon Europe funding guarantee (SYMPHONY; PI Bowman; grant number: EP/Y031059/1), and a Royal Society University Research Fellowship (PI Bowman; grant number: URF\R1\231631). J.B. is supported by an NWO Veni fellowship (VI.Veni.242.199). This research has used data obtained at the Mercator Observatory which receives funding from the Research Foundation – Flanders (FWO) (grant agreements I000325N and I000521N). This work presents results from the European Space Agency space mission Gaia. Gaia data are being processed by the Gaia Data Processing and Analysis Consortium (DPAC). Funding for the DPAC is provided by national institutions, in particular the institutions participating in the Gaia multilateral agreement.

DATA AVAILABILITY

The TESS data used in this work are publicly available from the MAST archive: https://archive.stsci.edu/missions-and-data/tess. The Hermes spectra used in this work are available from the archive: https://www.mercator.iac.es/instruments/hermes/archive/. The GAIA data used in this work are publicly available via the Gaia website: https://gea.esac.esa.int/archive/. The Padova database of stellar evolutionary tracks and isochrones are publicly available via the website: https://stev.oapd.inaf.it/cgi-bin/cmd. This research has made use of the SIMBAD database, operated at CDS, Strasbourg, France; the SAO/NASA Astrophysics Data System; and the VizieR catalogue access tool, CDS, Strasbourg, France.

For the purpose of open access, the authors have applied a CC BY licence to the author-accepted manuscript version: https://arxiv.org/abs/TBD. Data products that support the results in this paper are publicly available via the Zenodo repository: https://zenodo.org/records/TBD.

REFERENCES

Abdul-Masih M., et al., 2020, Nature, 580, E11
Aerts C., Tkachenko A., 2024, A&A, 692, R1
Aerts C., Thoul A., Daszyńska J., Scuflaire R., Waelkens C., Dupret M. A., Niemczura E., Noels A., 2003, Science, 300, 1926
Aerts C., Christensen-Dalsgaard J., Kurtz D. W., 2010, Asteroseismology, doi:10.1007/978-1-4020-5803-5.
Aerts C., et al., 2018, ApJS, 237, 15
Alfonso-Garzón J., Domingo A., Mas-Hesse J. M., Giménez A., 2012, A&A, 548, A79
Aller A., Lillo-Box J., Jones D., Miranda L. F., Barceló Forteza S., 2020, A&A, 635, A128
Auvergne M., et al., 2009, A&A, 506, 411
Balona L. A., et al., 2011, MNRAS, 413, 2403
Banyard G., Sana H., Mahy L., Bodensteiner J., Villaseñor J. I., Evans C. J., 2022, A&A, 658, A69
Baran A. S., Koen C., 2021, Acta Astron., 71, 113
Berthomieu G., Gonczi G., Graff P., Provost J., Rocca A., 1978, A&A, 70, 597
Bodensteiner J., Shenar T., Sana H., 2020a, A&A, 641, A42
Bodensteiner J., et al., 2020b, A&A, 641, A43
Bodensteiner J., et al., 2023, A&A, 680, A32
Bodensteiner J., et al., 2025, arXiv e-prints, p. arXiv:2502.02641
Borucki W. J., et al., 2010, Science, 327, 977
Bouabid M. P., Dupret M. A., Salmon S., Montalbán J., Miglio A., Noels A., 2013, MNRAS, 429, 2500
Bowman D. M., 2017, Amplitude Modulation of Pulsation Modes in Delta Scuti Stars, doi:10.1007/978-3-319-66649-5.
Bowman D. M., 2020, Frontiers in Astronomy and Space Sciences, 7, 70
Bowman D. M., 2023, Ap&SS, 368, 107
Bowman D. M., Kurtz D. W., 2018, MNRAS, 476, 3169
Bowman D. M., Michielsen M., 2021, A&A, 656, A158
Bowman D. M., et al., 2019, Nature Astronomy, 3, 760
Bowman D. M., et al., 2022, A&A, 658, A96
Bowman D. M., Van Daele P., Michielsen M., Van Reeth T., 2024, A&A, 692, A49
Bradley P. A., Guzik J. A., Miles L. F., Uytterhoeven K., Jackiewicz J., Kinemuchi K., 2015, AJ, 149, 68
Brasseur C. E., Phillip C., Fleming S. W., Mullally S. E., White R. L., 2019, Astrocut: Tools for creating cutouts of TESS images, Astrophysics Source Code Library, record ascl:1905.007 (ascl:1905.007)
Breeden C., et al., 2024, JAAVSO, 52, 67
Bressan A., Marigo P., Girardi L., Salasnich B., Dal Cero C., Rubele S., Nanni A., 2012, MNRAS, 427, 127
Brott I., et al., 2011, A&A, 530, A115
Burssens S., Bowman D. M., Aerts C., Pedersen M. G., Moravveji E., Buysschaert B., 2019, MNRAS, 489, 1304
Burssens S., et al., 2020, A&A, 639, A81
Burssens S., et al., 2023, Nature Astronomy, 7, 913
Chen Y., Bressan A., Girardi L., Marigo P., Kong X., Lanza A., 2015, MNRAS, 452, 1068
De Cat P., 2007, Communications in Asteroseismology, 150, 167
Dias W. S., Monteiro H., Moitinho A., Lépine J. R. D., Carraro G., Paunzen E., Alessi B., Villela L., 2021, MNRAS, 504, 356
Dupret M.-A., Thoul A., Scuflaire R., Daszyńska-Daszkiewicz J., Aerts C., Bourge P.-O., Waelkens C., Noels A., 2004, A&A, 415, 251
Dziembowski W., 1977, Acta Astronomica, 27, 203
Dziembowski W. A., Pamiatnykh A. A., 1993, MNRAS, 262, 204
Dziembowski W. A., Moskalik P., Pamyatnykh A. A., 1993, MNRAS, 265, 588
Fouesneau M., et al., 2023, A&A, 674, A28
Frémat Y., 2024, in Babusiaux C., Reylé C., eds, EES2023: Proceedings of the Evry Schatzman School. p. 59 (arXiv:2411.04887), doi:10.48550/arXiv.2411.04887
Fritzewski D. J., Vanrespaille M., Aerts C., Guo Z., Hey D., De Ridder J., 2025, A&A, 698, A253
Fritzewski D. J., Kemp A., Li G., Aerts C., 2026, A&A, 706, A131
Gaia Collaboration et al., 2016a, A&A, 595, A1
Gaia Collaboration et al., 2016b, A&A, 595, A2
Gaia Collaboration et al., 2018, A&A, 616, A1
Gaia Collaboration et al., 2023, A&A, 674, A1
Gray D. F., 2021, The Observation and Analysis of Stellar Photospheres, 4 edn. Cambridge University Press
Guo Y., et al., 2021, The Astrophysical Journal Supplement Series, 257, 54
Handler G., 2009, MNRAS, 398, 1339
Hastings B., Wang C., Langer N., 2020, A&A, 633, A165
Hotelling H., 1932, Journal of Educational Psychology, 24, 417
Howell S. B., et al., 2014, PASP, 126, 398
Hubeny I., Lanz T., 1995, ApJ, 439, 875
Johnston C., 2021, A&A, 655, A29
Johnston C., Tkachenko A., Aerts C., Molenberghs G., Bowman D. M., Pedersen M. G., Buysschaert B., Pápics P. I., 2019a, MNRAS, 482, 1231
Johnston C., Aerts C., Pedersen M. G., Bastian N., 2019b, A&A, 632, A74
Kippenhahn R., Weigert A., Weiss A., 2013, Stellar Structure and Evolution, doi:10.1007/978-3-642-30304-3.
Kurtz D. W., Shibahashi H., Murphy S. J., Bedding T. R., Bowman D. M., 2015, MNRAS, 450, 3015
Labadie-Bartz J., Carciofi A. C., Henrique de Amorim T., Rubio A., Luiz Figueiredo A., Ticiani dos Santos P., Thomson-Paressant K., 2022, AJ, 163, 226
Labadie-Bartz J., et al., 2025, A&A, 699, A82
Langer N., 2012, ARA&A, 50, 107

Langer N., Kudritzki R. P., 2014, A&A, 564, A52
Lanz T., Hubeny I., 2007, ApJS, 169, 83
Laur J., Kolka I., Eenmäe T., Tuvikene T., Leedjärv L., 2017, A&A, 598, A108
Lecoanet D., Bowman D. M., Van Reeth T., 2022, MNRAS, 512, L16
Lenz P., Breger M., 2005, Communications in Asteroseismology, 146, 53
Li G., Van Reeth T., Bedding T. R., Murphy S. J., Antoci V., Ouazzani R.-M., Barbara N. H., 2020, MNRAS, 491, 3586
Lightkurve Collaboration et al., 2018, Lightkurve: Kepler and TESS time series analysis in Python, Astrophysics Source Code Library (ascl:1812.013)
Loumos G. L., Deeming T. J., 1978, Ap&SS, 56, 285
Ma L., Johnston C., Bellinger E. P., de Mink S. E., 2024, ApJ, 966, 196
Marchant P., Bodensteiner J., 2024, ARA&A, 62, 21
Mathis S., Prat V., 2019, A&A, 631, A26
Miglio A., Montalbán J., Dupret M.-A., 2007, MNRAS, 375, L21
Miglio A., Montalbán J., Noels A., Eggenberger P., 2008, MNRAS, 386, 1487
Moravveji E., Aerts C., Pápics P. I., Triana S. A., Vandoren B., 2015, A&A, 580, A27
Moravveji E., Townsend R. H. D., Aerts C., Mathis S., 2016, ApJ, 823, 130
Nardini F., Bodensteiner J., Sana H., Mahy L., Deshmukh K., Bowman D. M., 2025, MNRAS, 540, 2009
Nazé Y., Britavskiy N., Labadie-Bartz J., 2024, A&A, 689, A320
Nova S. S., Richardson N. D., Labadie-Bartz J., Garcia Flores S., 2025, arXiv e-prints, p. arXiv:2512.08214
Offner S. S. R., Moe M., Kratter K. M., Sadavoy S. I., Jensen E. L. N., Tobin J. J., 2023, in Inutsuka S., Aikawa Y., Muto T., Tomida K., Tamura M., eds, Astronomical Society of the Pacific Conference Series Vol. 534, Protostars and Planets VII. p. 275 (arXiv:2203.10066), doi:10.48550/arXiv.2203.10066
Pápics P. I., 2012, Astronomische Nachrichten, 333, 1053
Pápics P. I., et al., 2017, A&A, 598, A74
Paxton B., Bildsten L., Dotter A., Herwig F., Lesaffre P., Timmes F., 2011, ApJS, 192, 3
Paxton B., et al., 2013, ApJS, 208, 4
Paxton B., et al., 2015, ApJS, 220, 15
Paxton B., et al., 2018, ApJS, 234, 34
Pecaut M. J., Mamajek E. E., 2013, ApJS, 208, 9
Pedersen M. G., et al., 2021, Nature Astronomy, 5, 715
Raskin G., et al., 2011, A&A, 526, A69
Ricker G. R., et al., 2015, Journal of Astronomical Telescopes, Instruments, and Systems, 1, 014003
Rivinius T., Klement R., 2026, in Encyclopedia of Astrophysics. pp 430–448 (arXiv:2411.06882), doi:10.1016/B978-0-443-21439-4.00042-0
Rivinius T., Baade D., Štefl S., 2003, A&A, 411, 229
Rivinius T., Carciofi A. C., Martayan C., 2013, A&ARv, 21, 69
Rivinius T., Baade D., Carciofi A. C., 2016, A&A, 593, A106
Saio H., 2013, in Goupil M., Belkacem K., Neiner C., Lignières F., Green J. J., eds, , Vol. 865, Lecture Notes in Physics, Berlin Springer Verlag. p. 159, doi:10.1007/978-3-642-33380-4_8
Sana H., et al., 2012, Science, 337, 444
Schneider F. R. N., 2025, arXiv e-prints, p. arXiv:2509.18421
Schneider F. R. N., Langer N., de Koter A., Brott I., Izzard R. G., Lau H. H. B., 2014, A&A, 570, A66
Scott L. J. A., Bowman D. M., 2026, MNRAS, 545, staf2174
Semaan T., Hubert A. M., Zorec J., Gutiérrez-Soto J., Frémat Y., Martayan C., Fabregat J., Eggenberger P., 2018a, A&A, 613, A70
Semaan T., Hubert A. M., Zorec J., Gutiérrez-Soto J., Frémat Y., Martayan C., Fabregat J., Eggenberger P., 2018b, A&A, 613, A70
Shenar T., et al., 2020, A&A, 639, L6
Shi X.-d., Qian S.-b., Zhu L.-y., Liu L., Li L.-j., Zang L., 2023, ApJS, 265, 33
Sigut T. A. A., Ghafourian N. R., 2023, ApJ, 948, 34
Southworth J., Bowman D., 2025, arXiv e-prints, p. arXiv:2509.08426
Stankov A., Handler G., 2005, ApJS, 158, 193
Stassun K. G., et al., 2018, AJ, 156, 102
Szewczuk W., Daszyńska-Daszkiewicz J., 2018, MNRAS, 478, 2243
Szewczuk W., Walczak P., Daszyńska-Daszkiewicz J., 2021, MNRAS, 503, 5894
Talon S., Zahn J.-P., Maeder A., Meynet G., 1997, A&A, 322, 209
Thompson S. E., et al., 2012, ApJ, 753, 86
Townsend R. H. D., Teitler S. A., 2013, MNRAS, 435, 3406
Townsend R. H. D., Owocki S. P., Howarth I. D., 2004, MNRAS, 350, 189
Van Daele P. J., et al., 2026, arXiv e-prints, p. arXiv:2605.15757
Van Reeth T., Tkachenko A., Aerts C., 2016, A&A, 593, A120
Van Reeth T., et al., 2018, A&A, 618, A24
Vandersnickt J., Vanlaer V., Vanrespaille M., Aerts C., 2025, arXiv e-prints, p. arXiv:2511.21812
Vanlaer V., Bowman D. M., Burssens S., Bharati Das S., Bugnet L., Mathis S., Aerts C., 2025, A&A, 701, A5
Villaseñor J. I., et al., 2025, A&A, 698, A41
Walker G., et al., 2003, PASP, 115, 1023
Wang C., Langer N., Schootemeijer A., Castro N., Adscheid S., Marchant P., Hastings B., 2020, ApJ, 888, L12
Wang C., et al., 2023, A&A, 670, A43
Weiss W. W., et al., 2014, PASP, 126, 573
Zhang X. B., Luo C. Q., Fu J. N., 2012, AJ, 144, 86
Zimmerman M. K., Thompson S. E., Mullally F., Fuller J., Shporer A., Hambleton K., 2017, The Astrophysical Journal, 846, 147
de Mink S. E., Sana H., Langer N., Izzard R. G., Schneider F. R. N., 2014, The Astrophysical Journal, 782, 7

APPENDIX A: NOTES ON INDIVIDUAL SYSTEMS

A1 Pulsating Be stars

NGC 1960 101: the light curve and frequency spectrum of this Be star are an example of perhaps the most extreme outburst within the sample. The light curve is shown in the first row of Fig. 4, and displays strong sector-to-sector variability. In the three consecutive TESS sectors shown, each exhibits a prominent increase in brightness near the beginning. We investigated potential instrumental causes and possible contamination from bright nearby sources, but found no evidence for either. Given the classification of this target as a Be star based on strong Hα emission, the large photometric variability is likely related to the presence of a decretion disc and repeated outbursts. The frequency spectrum is dominated by an upward trend at very low frequency (below 1 d^{-1}) caused by the intermittent quasi-periodic outbursts. For this reason, there are no dominant gravity-mode frequencies or frequency groups. We note that, other than PCA detrending, no additional spline detrending was performed for the TESS light curves of this star due to its large-scale variability. Regarding the spectra, the bottleneck shape of the Hα emission line, together with its low projected rotational velocity, means that this Be star is likely viewed close to pole-on. The amplitude of the emission line is extremely high, and there is a decrease in flux between the first spectra taken in 2016 and the last one taken in 2024, indicating that the decretion disc is transient.

BD+56 566: Is the only pulsating Be star in *h* and χ Per and exhibits the strongest long-term photometric variability across all three available TESS sectors during 2019 (sector 18), 2022 (sector 58) and 2024 (sector 85). The frequency spectrum of the non-detrended light curve is dominated by the long-term trends, but multi-periodic gravity-modes and frequency groups at about 1 d^{-1} and 2.5 d^{-1} are evident in the frequency spectrum of the detrended light curve (see second row of Fig. 4). The two available Hermes spectra were obtained in March 2024 with a separation of only 2 d, which is too short to reveal any outburst signatures via changes in the emission lines. The unequal peak heights of Hα might be caused by the V/R cycle, but the lack of spectral coverage does not allow us to confirm if there is spectroscopic variability.

NGC 457 198: This Be star has the longest-period pulsations and smaller amplitude changes due to beating compared to the rest of the sample. There are four dominant frequency groups in the frequency spectrum (see third row of Fig. 4), and all of them are below 2 d^{-1}. The first Hermes spectrum was taken in 2016 and shows lower amplitude Hα emission compared to the additional 17 spectra, which show little-to-no variability until the last spectrum taken in 2022.

EM GGA 54:* The Hermes spectra show signatures of a V/R cycle, but with only four epochs, we lack the coverage to establish the variability cycle. The largest difference in Hα emission is observed between the last two spectra, which were obtained one year apart.

NGC 457 275: Two of the Hermes spectra for this star were obtained contemporaneously with TESS sector 18 in 2019. No long-term trends are seen in the light curve, and no variability is detected in the Hermes spectra across this 28-d time span (see fourth row of Fig. 4, which suggests that the star did not undergo any significant outbursts in this time. The additional Hermes spectra span three years and do not show large variability in Hα . Moreover, the shape of Hα indicates that the star is seen almost pole-on.

NGC 457 153: The bottle-neck shape of Hα in this Be star indicates an inclination angle of around 40 deg (Sigut & Ghafourian 2023), and there are no signs of variability across the 4-yr time span. As shown in the sixth row of Fig. 4, there are no long-term trends in the two TESS sectors available (sectors 18 and 58). The frequency spectra show two peaks at about 0.8 and 1.5 d, which indicate that the frequency groups in this star contain fewer gravity modes.

NGC 457 128: There is no evidence of long-term photometric variability in the two available TESS sectors (18 and 58). However, the multi-epoch Hermes spectra spanning almost 3 yr show time-dependent emission in the Balmer lines (see seventh row of Fig. 4). Several Hermes spectra obtained between 2017 and 2020 reveal emission features only in the four epochs observed in 2019, suggesting a possible mass-ejection event that supplied a decretion disc for roughly five months (from August to November 2019). By January 2020, the emission had disappeared and Hα returned to being in absorption. Sector 18 of the TESS mission occurred in November 2019, but no brightening or fading occurred during this time, and only multi-periodic gravity-mode pulsations are evident. The small amplitude of the Hα emission (around 0.2 in normalised flux) suggests that the mass-ejection-induced brightness increase may not be sufficient to produce a visible flux increase in the broad-band TESS light curve.

NGC 457 91: This Be star is another example of long-term photometric variability in both available TESS sectors. In the non-detrended sector 58 TESS light curve, which is shown in the eighth row of Fig. 4, there are small fading and brightening events. While the frequency groups remain consistent between the two TESS sectors, the amplitudes of the pulsation modes are lower in sector 18 compared to sector 58. One of the Hermes spectra was taken in the same month of sector 58, but no variability in Hα is detected compared to the other available spectra. The Hermes spectra span from 2017 to 2020 and show no strong variability apart from a slight decrease in amplitude of Hα between the first and second year of observations.

NGC 581 49: This Be star has the smallest pulsation amplitudes in the light curve and frequency spectrum in our sample. Sector 58 shows long-term photometric variability (see ninth row of Fig. 4), but it depends on which aperture mask is used, so this is deemed to be instrumental and not astrophysical in origin.

NGC 960 27: There are seven TESS sectors available for this star, with the three consecutive sectors 43, 44, and 45 shown in the tenth row of Fig. 4. The larger amount of TESS data is reflected in the dense frequency groups in the frequency spectrum, with the dominant gravity-mode pulsations of about 2.2 d^{-1}. The twelve Hermes spectra obtained between 2016 and 2024 show a steady increase in the amplitude of Hα , indicating continuous disc growth during this time.

EM GGA 56:* This star has the highest projected rotational velocity of all the Be stars in our sample with $v \sin i = 360$ km s^{-1}. It is also among those with the largest number of frequency groups (five), with the highest-frequency one detected at 7 d^{-1}, as shown in the eleventh row of Fig. 4. The eight available Hermes spectra show no variability in Hα across 516 d, although the last spectrum was obtained in 2021, which pre-dates the TESS data.

A2 Photometric binaries

χ Per 2311: (also known as V621 Per), the TESS data are shown in the first row of Fig. 12. It was previously identified as an EB by Laur et al. (2017), but the system remains to be modelled to extract dynamical masses and radii. χ Per 2311 is the longest-period EB in our sample with an orbital period of 25.5237 ± 0.0054 d and an eccentricity of 0.26821 ± 0.00006 determined from spectroscopic RV analysis in Paper 1. The primary eclipses occur near the beginning and end of the 27-day period for the TESS sector 58, and the asymmetric time differences between secondary and primary eclipses support the high eccentricity. Additionally, one or both of the components is a pulsating star, with pulsating EBs invaluable for constraining stellar structure and evolution theory (see Southworth & Bowman 2025). χ Per 2311 suffers from a moderate level of contamination, so whilst the spectroscopic and photometric solutions for binarity are in agreement, it is not possible with current data sets to ascertain the origin of the pulsations.

NGC 457 37: (also known as BD+57 249) Zhang et al. (2012) were the first to identify the system as an EB and determine the orbital period of P_{zhang} = 4.44768 ± 0.00008 d using ground-based two-colour photometry. This is consistent with the spectroscopic binary period determined in Paper 1, which is P_{spec} = 4.4475 ± 0.0003 d, as well as the photometric period found in this work of P_{phot} = 4.447500 ± 0.000001 d. The similar eclipse depths of NGC 457 37 indicate it contains two stars of similar brightness in a circular orbit.

NGC 457 85: (also known as V765 Cas) is the only EB in our sample that is also SB2. It was first identified as an EB by Alfonso-Garzón et al. (2012) and it was later modelled by Breeden et al. (2024) using photometry from different instruments (including TESS), as well as undergoing isochrone fitting. Based on the shape of the light curve and the location of the star on the CMD, the authors classified it as a β Lyr-type binary. The analysis of Breeden et al. (2024) confirms the period of 1.715779 d from Alfonso-Garzón et al. (2012), which is also consistent with the spectroscopic binary period of P_{spec} = 1.7160 ± 0.0002 d from Paper 1 and P_{phot} = 1.714099 ± 0.000004 d determined in this work.

EM GGA 52:* also previously identified as an EB by Laur et al. (2017) but no modelling has been performed. The spectroscopic period of P_{spec} = 2.2507 ± 0.0002 d determined in Paper 1 was half the photometric period of P_{phot} = 4.502164 ± 0.000003 d derived in this work. The light curve in Fig. 12 demonstrates that the spectroscopic solution is an alias of the true photometric binary period.

NGC 1960 134: this is the only photometric binary in our sample that was not previously known in the literature. It is a short-period binary system with P_{spec} = 8.8600 ± 0.0021 d and high eccentricity of e =0.54431 ± 0.00015 according to Paper 1. Its TESS light curve is shown in the bottom row of Fig. 12, and shows periodic brightening on the same time scale as the spectroscopic orbital period. The high eccentricity is likely sufficient to cause significant tidal distortion at

periastron passage and give rise to a periodic brightening. Such systems have often been called "heartbeat stars" due to the resemblance of the light curve to an electrocardiogram (Thompson et al. 2012; Zimmerman et al. 2017). Binary tidal forces also induce pulsations at integer harmonics of the orbital period. Once these harmonics are removed, it is possible to remove the binary signal from the light curve and inspect to see if there are signs of pulsation variability. Indeed, once removed, the light curve shows signs of pulsations, and the peaks in the dFT between 2 and 3 d^{-1} are likely caused by the pulsation. This suggests that one of the components of the binary system is either an SPB or a β Cep.

A3 Rotational modulation stars

NGC 1960 8: this is one of the three SB2 systems identified in Paper 1, and as the spectra were not disentangled, no $v \sin i$ measurement could be obtained. The spectroscopic and photometric periods of $P_{\rm spec} = 2.4973 \pm 0.0002$ d and $P_{\rm phot} = 2.49853 \pm 0.00001$ d are identical within their respective confidence intervals, which demonstrates that the star with rotational modulation is synchronised with the orbit.

NGC 1960 16: is an SB1 system that lies on the bisector in Fig. 11 such that its spectroscopic and dominant photometric periods agree, but it is not classified as a photometric binary. The sinusoidal shape of the light curve and of the phase-folded light curve are typical of a star with rotational modulation, but since it is not perfectly periodic, this could mean either variable amplitude abundance patterns or that this star is in fact a multi-periodic pulsator. The absorption lines in the spectra did not show line profile variability apart from RV shifts due to binarity, and the peak-to-peak RV variability shift exceeds 43 km s^{-1}. If this is a pulsator, then it seems rather coincidental that the dominant pulsation mode frequency is near the binary frequency. Whereas, if this is a star with rotational modulation, it is thus synchronised with the orbit.

χ Per 2185: is the other SB1 system in our sample that lies on the bisector in Fig. 11, but it is not classified as a photometric binary based on its TESS light curve in this work. The photometric and spectroscopic periods of $P_{\rm phot} = 1.45924 \pm 0.00004$ d and $P_{\rm spec} = 1.5483 \pm 0.0002$ d are similar but not compatible considering their respective confidence intervals. The sinusoidal shape of the TESS light curve and especially of the phase-folded light curve, which are shown in Fig. 13, is tentative for classifying this star as having rotational modulation. Since there is only one consecutive TESS sector available, this limits our frequency resolution. Moreover, the S/N ratios of the available Hermes spectra are low compared to most of the stars in our sample, and the peak-to-peak RV variability is only ~ 29 km s^{-1}. Therefore, the argument that the star is rotationally synchronised with the orbital system and that the spectroscopic period is caused by chemical abundance anomalies is tentative.

APPENDIX B: ADDITIONAL TABLES AND FIGURES

This paper has been typeset from a TEX/LATEX file prepared by the author.

Table B1. Name and properties of the 82 stars in our sample. The spectral type and binary status were determined in Paper 1. The last two columns are the contamination ratio (values higher than 1 mean that the majority of the flux is coming from a contaminating source) and the type of pulsators.

SIMBAD ID	TIC ID	V [mag]	SpT	Binary status	$C_{\rm ratio}$	Class
Cluster: h and χ Persei		TESS Sectors: 18, 58, 85				
BD+56 515	264730455	8.53	B2 V	Single	1.9	β Cep
BD+56 566	348444454	10.16	B1e V	Single	0.12	Be
χ Per 2114	348444627	11.04	B2 V	Single	4.5	β Cep†
χ Per 2185	348607492	10.92	B5 V	SB1	0.51	Rot Modulation
χ Per 2235	348607658	8.40	B1 V	Single	3.4	β Cep†
χ Per 2246	348607672	9.98	B1V	Single	7.0	β Cep†
χ Per 2255	348607731	10.71	B2 V	SB1	7.4	β Cep†
χ Per 2296	348607543	8.53	B1 II-III	Single	0.71	β Cep
χ Per 2299	348607604	8.32	B1 II-III	Single	1.4	β Cep†
χ Per 2311	348607572	9.40	B0 V	SB1	3.0	EB
χ Per 2392	348607862	10.71	B2 V	SB2	0.58	constant
HD 14052	264612788	7.79	B1 II III	SB1	0.30	β Cep
h Per 0622	264612967	10.89	B2 II III	Single	1.0	β Cep
h Per 0843	264730428	8.38	B1 V	SB1	0.59	β Cep
h Per 0864	264730166	9.16	B2 V	Single	0.87	β Cep
h Per 0929	264730591	10.32	B2 V	Single	2.2	β Cep†
h Per 0936	264730544	10.44	B0 V	Single	5.5	β Cep†
h Per 0978	264730588	10.68	B2 II III	Single	4.5	-
h Per 0980	264730498	9.75	B0 V	SB1	7.2	-
h Per 0992	264730502	10.00	B1 II III	Single	11.5	-
h Per 1004	264730535	10.91	B2 V	SB1	12.9	-
h Per 1078	264730358	9.82	B1 V	Single	16.9	-
h Per 1085	264730539	10.47	B1 V	SB1	5.5	-
h Per 1116	264730427	9.29	B1 V	Single	10.1	-
h Per 1132	264730392	8.48	B2 II III	Single	3.4	-
h Per 1133	264730365	9.04	B1 II-III	Single	5.1	-
Cluster: NGC 457		TESS Sectors: 18, 58				
NGC 457 6	332499085	10.60	B3e V	SB1	3.1	Be†
NGC 457 7	332499065	10.95	B5 V	SB1	2.5	-
NGC 457 8	332499097	10.02	B1 V	SB1	0.97	β Cep
NGC 457 14	332499244	10.20	B1e V	SB1	2.4	Be†
NGC 457 19	332499278	9.51	B1 II-III	SB1	0.67	β Cep
NGC 457 33	332498935	10.33	B2 V	Single	0.25	β Cep
NGC 457 34	332499026	10.74	B5 V	Single	2.3	hybrid
NGC 457 37	332499008	9.83	B2 V	SB1	0.86	EB
NGC 457 54	332499331	10.18	B2 V	SB1	0.19	β Cep
NGC 457 85	332499083	10.78	B5 V	SB2	0.19	EB
NGC 457 91	332499409	11.30	B5e V	SB1	0.38	Be
NGC 457 100	332499478	10.61	B2 V	SB1	11.8	-
NGC 457 120	332498822	9.93	B0 V	Single	0.14	constant
NGC 457 128	332489861	9.72	B2e V	Single	0.06	Be
NGC 457 153	332489770	9.48	B1e V	Single	0.02	Be
NGC 457 154	332489761	11.18	B5 V	SB1	0.30	hybrid†
NGC 457 198	332490249	9.46	B2e V	Single	0.13	Be
NGC 457 275	332489539	9.85	B3e V	Single	0.02	Be
HD 236695	332497979	9.50	B2 II III	Single	0.04	β Cep
Cluster: NGC 581		TESS Sectors: 18, 25, 58, 85				
NGC 581 49	389771251	11.76	B2e V	Single	1.2	Be
NGC 581 35	389771025	10.45	B3 V	SB1	0.19	β Cep
NGC 581 59	389771267	11.45	B3 V	SB1	1.9	β Cep†
NGC 581 70	389771358	11.74	B5 V	Single	22.3	hybrid†
NGC 581 73	389771312	10.59	B5 V	Single	1.5	hybrid†
NGC 581 162	389770884	11.22	B2 V	Single	0.23	β Cep
NGC 581 111	389974549	11.84	B5 V	Single	0.30	-
NGC 581 122	389771239	11.00	B2 V	SB1	36.1	β Cep†
TYC 4031 2100 1	389766903	11.65	B2 V	Single	0.19	-
BD+59 273	389771132	9.03	B1 V	Single	1.0	β Cep†
EM* GGA 52	389771144	11.22	B3 V	SB1	0.73	EB
EM* GGA 54	389771271	11.27	B0e V	Single	5.0	Be
EM* GGA 56	389771456	11.35	B5e V	Single	0.50	Be
V* V1122 Cas	389771376	9.71	B3e V	SB1	9.3	-

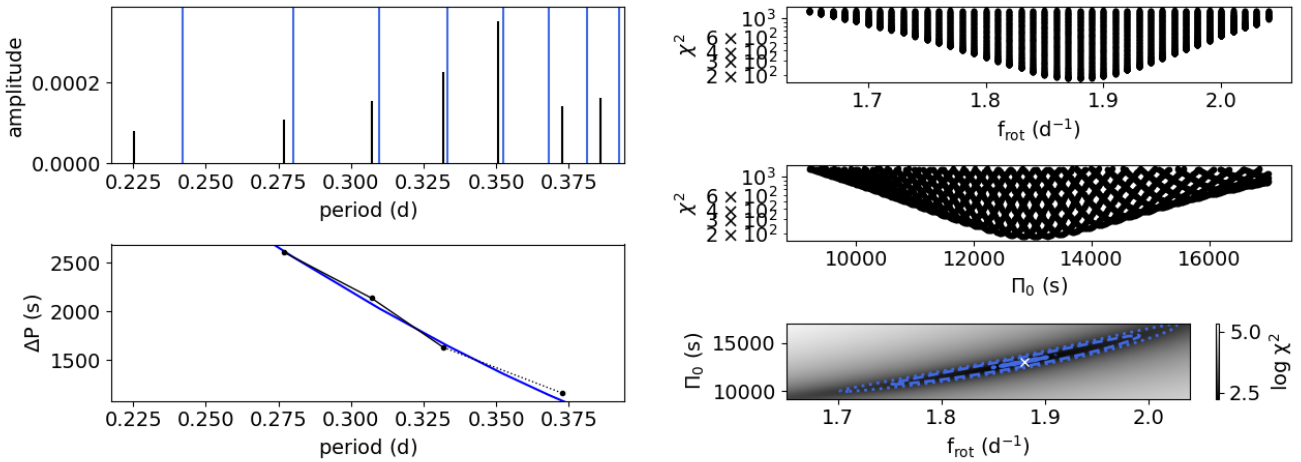

Figure B1. The group 1 period spacing pattern ($\ell = 1$, $m = 1$) with the AMIGO best-fit in the left panels, and the 1D and 2D χ^2 distributions of Π_0 and $f_{\rm rot}$ in the right panels for NGC 1960 81.

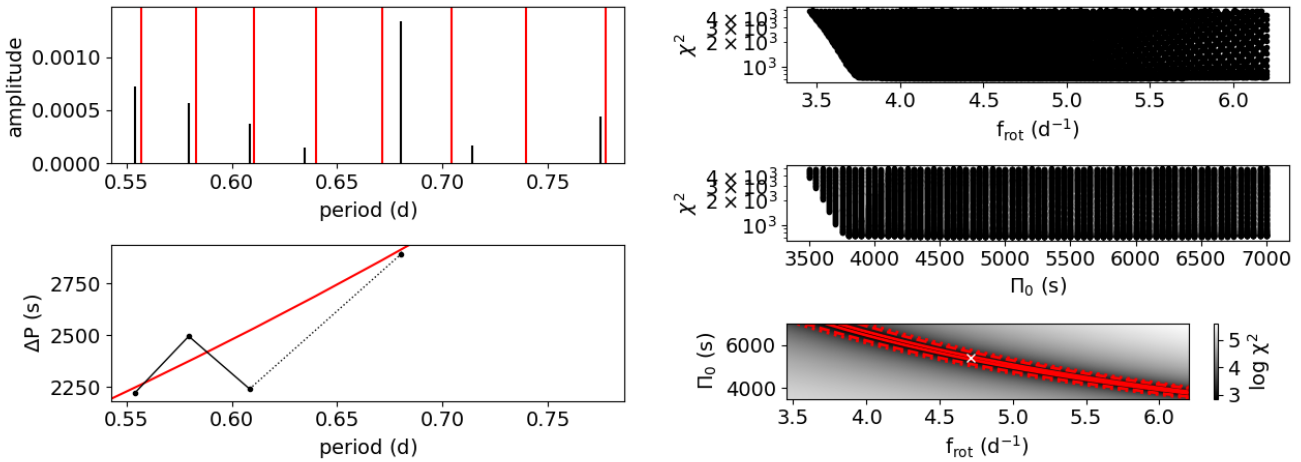

Figure B2. Same as Fig. B1 but for the period spacing pattern of Group 2 with mode geometry $\ell = 5$ $m = -1$ for NGC 1960 81.

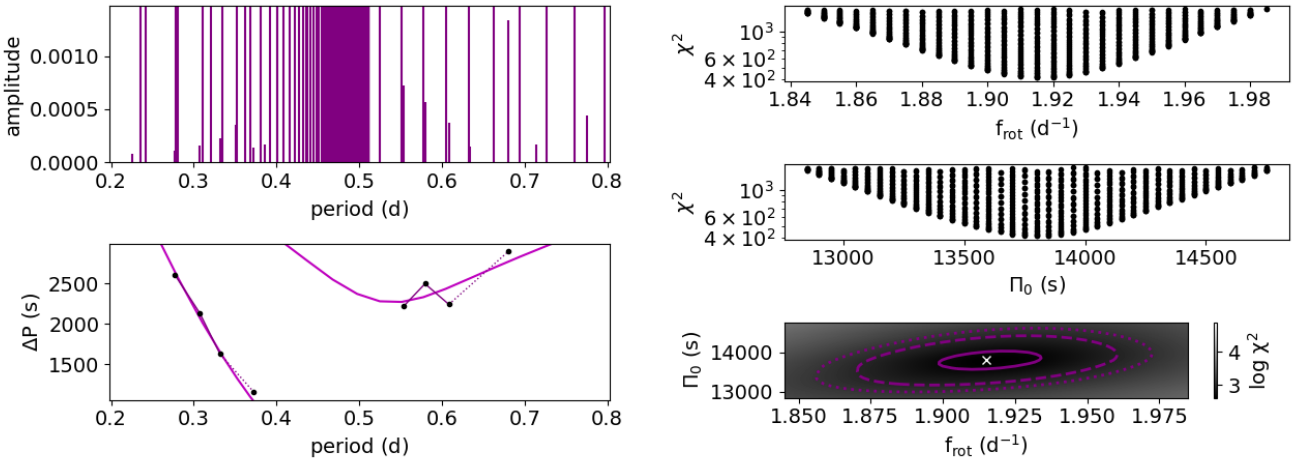

Figure B3. Same as Fig. B1 but for a combined fit of group 1 and group 2 period spacing patterns of NGC 1960 81, with mode geometries of $\ell = 1$, $m = 1$ and $\ell = 5$, $m = -1$, respectively.

Table B1 – *continued*

SIMBAD ID	TIC ID	V [mag]	SpT	Binary status	C_{ratio}	Class
Cluster: NGC 1960		TESS Sectors: 19, 43, 44, 45, 59, 71, 73				
NGC 1960 003	115722242	10.72	B7 V	Single	2.1	-
NGC 1960 008	115722132	9.36	B2 V	SB2	1.3	Rot Modulation
NGC 1960 009	115722123	9.13	B1 V	SB1	0.97	-
NGC 1960 013	115722060	10.80	B7 V	Single	1.3	-
NGC 1960 014	115722047	10.68	B7 V	Single	1.3	-
NGC 1960 016	115722162	8.79	B2 V	SB1	0.15	Rot Modulation
NGC 1960 018	115722189	10.78	B5 III	Single	2.2	hybrid†
NGC 1960 021	115722282	9.60	B2 V	Single	1.9	β Cep†
NGC 1960 023	115722303	8.96	B3 V	Single	0.45	β Cep
NGC 1960 027	115722156	9.58	B2e V	SB1	0.19	Be
NGC 1960 038	115721955	9.92	B3 V	Single	0.20	β Cep
NGC 1960 047	115559839	10.44	B5e V	Single	0.64	Be†
NGC 1960 048	115559789	9.36	B3 V	Single	0.31	β Cep
NGC 1960 061	115722319	9.09	B2 V	Single	0.07	β Cep
NGC 1960 081	115559920	9.99	B2 V	Single	0.16	SPB
NGC 1960 086	115559710	10.65	B7 V	Single	0.44	hybrid
NGC 1960 087	115559692	10.65	B5 V	Single	0.25	hybrid
NGC 1960 091	115559630	10.37	B5 V	Single	0.20	SPB
NGC 1960 092	115559595	10.96	B9 V	Single	0.42	hybrid δ Scuti
NGC 1960 101	115722396	9.14	B2e V	Single	0.03	Be
NGC 1960 109	115642252	10.70	B3 V	SB1	0.85	-
NGC 1960 134	115730751	10.39	B2 V	SB1	0.06	heartbeat
NGC 1960 138	115642245	8.94	B2 V	Single	0.19	β Cep

Notes. †Stars for which we tentatively classify the pulsation class, but the contamination level is high.

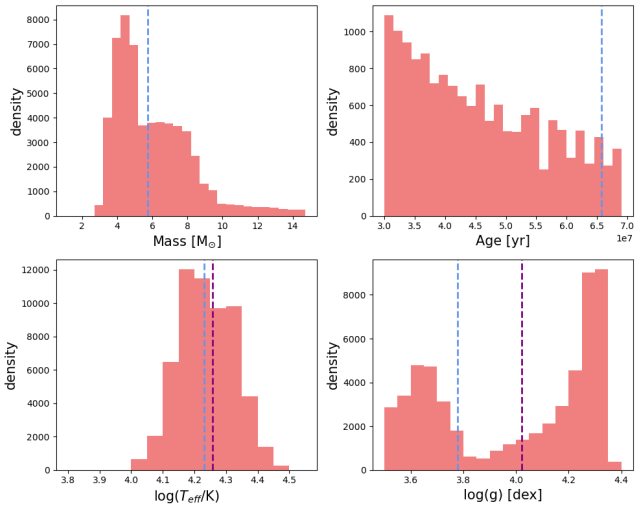

Figure B4. Same as Fig. 9 but for the modelling of the group 2 period spacing pattern.

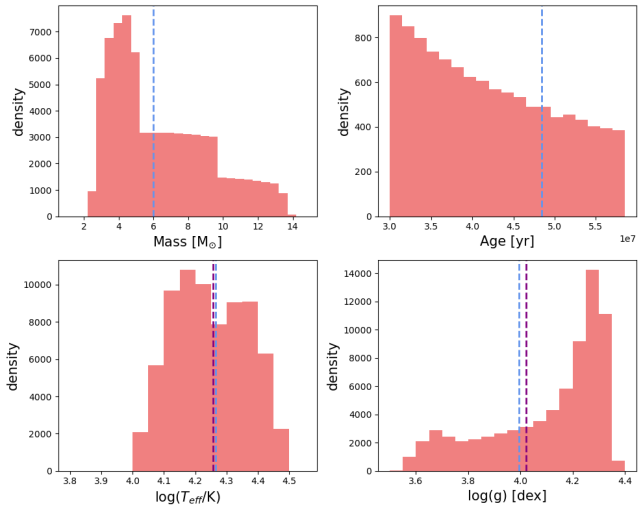

Figure B5. Same as Fig. 9 but for the modelling of the combined fit of group 1 and group 2 period spacing patterns.

Table B2. IDs, significant frequencies, amplitudes and phases of the 22 β Cep, SPBs and hybrids identified in the four different clusters.

simbad ID	TIC ID	f [d^{-1}]	A [mmag]	ϕ
BD+56 515	264730455	0.83409(8)	0.82(2)	0.15 ± 0.23
		1.38075(6)	1.09(2)	0.62 ± 0.17
		2.12101(6)	1.13(2)	0.76 ± 0.17
chi Per 2296	348607543	0.74476(7)	3.63(7)	0.86 ± 0.20
HD 14052	264612788	-	-	-
h Per 0622	264612967	0.38338(4)	1.20(1)	0.32 ± 0.13
		5.8236(3)	0.16(1)	0.14 ± 0.97
h Per 0843	264730428	2.1400(2)	0.21(1)	0.86 ± 0.54
		3.1849(3)	0.14(1)	0.80 ± 0.80
		4.50047(6)	0.70(1)	0.39 ± 0.16
		9.1816(3)	0.16(1)	0.90 ± 0.75
h Per 0864	264730166	0.22612(5)	1.58(2)	0.07 ± 0.11
		1.25688(8)	0.75(2)	0.05 ± 0.23
		7.0492(5)	0.13(2)	0.47 ± 1.30
		14.1087(4)	0.14(2)	0.03 ± 1.22
NGC 457 8	332499097	0.44901(3)	2.41(2)	0.65 ± 0.10
		5.34021(1)	8.64(2)	0.69 ± 0.03
		5.4331(3)	0.28(2)	0.21 ± 0.85
NGC 457 19	332499278	0.80020(7)	1.46(3)	0.05 ± 0.22
NGC 457 33	332498935	0.18151(5)	2.77(3)	0.99 ± 0.14
NGC 457 34	332499026	2.8012(1)	0.64(2)	0.96 ± 0.36
		5.34038(3)	2.59(2)	0.17 ± 0.09
NGC 457 54	332499331	1.0307(1)	0.34(1)	0.24 ± 0.42
HD 236695	332497979	0.38916(3)	3.74(3)	0.98 ± 0.09
		0.47512(5)	2.27(3)	0.70 ± 0.15
NGC 581 35	389771025	0.66973(7)	0.64(2)	0.96 ± 0.27
		1.43361(6)	0.86(2)	0.93 ± 0.20
NGC 581 162	389770884	1.0915(1)	0.52(2)	0.79 ± 0.45
		1.19255(6)	1.00(2)	0.74 ± 0.23
		2.7743(2)	0.28(2)	0.41 ± 0.81
NGC 1960 23	115722303	0.61977(5)	0.62(9)	0.88 ± 0.13
		1.7085(2)	0.17(9)	0.06 ± 0.47
		1.8380(2)	0.19(9)	0.90 ± 0.44
NGC 1960 38	115721955	0.6994(1)	0.22(7)	0.6 ± 0.32
		0.82496(9)	0.31(7)	0.49 ± 0.23
		1.5531(2)	0.19(7)	0.30 ± 0.38
		2.0437(2)	0.18(8)	0.96 ± 0.40
		2.1954(2)	0.17(8)	0.67 ± 0.42
		2.30293(4)	0.78(8)	0.16 ± 0.09
		19.2089(6)	0.05(7)	0.81 ± 1.42
		20.4141(4)	0.07(7)	0.43 ± 0.98
		27.4541(3)	0.09(7)	0.83 ± 0.77
		28.0289(6)	0.05(7)	0.18 ± 1.51
NGC 1960 48	115559789	0.4437(1)	0.16(6)	0.94 ± 0.35
		0.5567(2)	0.12(6)	0.01 ± 0.47
		2.3191(3)	0.09(6)	0.87 ± 0.64
		2.90732(3)	0.07(6)	0.58 ± 0.79
		3.5817(1)	0.18(6)	0.33 ± 0.32

Table B2 – *continued* Table continued from the previous one.

simbad ID	TIC ID	f [d^{-1}]	A [mmag]	ϕ
NGC 1960 61	115722319	0.41092(7)	0.75(1)	0.65 ± 0.19
		1.24597(7)	0.82(2)	0.54 ± 0.17
		1.2997(2)	0.37(2)	0.09 ± 0.42
		1.34674(1)	0.48(2)	0.77 ± 0.30
		1.44330(1)	0.44(2)	0.67 ± 0.33
		2.4956(3)	0.21(1)	0.58 ± 0.70
		2.6379(2)	0.25(1)	0.82 ± 0.57
		2.8708(4)	0.16(1)	0.25 ± 0.88
		5.0301(5)	0.11(1)	0.02 ± 1.26
		5.0976(5)	0.12(1)	0.31 ± 1.14
		6.4457(3)	0.19(1)	0.79 ± 0.76
		6.6540(6)	0.09(1)	0.21 ± 1.57
		7.2726(8)	0.07(1)	0.66 ± 1.99
		7.8251(4)	0.14(1)	0.98 ± 1.02
		10.2245(5)	0.11(1)	0.99 ± 1.24
		10.3646(4)	0.16(1)	0.38 ± 0.90
		10.5385(6)	0.09(1)	0.59 ± 1.51
NGC 1960 87	115559692	1.4779(1)	0.35(2)	0.83 ± 0.26
		2.8596(2)	0.207(8)	0.57 ± 0.38
		2.9619(2)	0.185(9)	0.78 ± 0.43
		3.0333(3)	0.122(8)	0.28 ± 0.65
		3.2161(3)	0.103(8)	0.16 ± 0.77
		4.4331(4)	0.10(1)	0.77 ± 0.89
		5.82025(8)	0.387(8)	0.21 ± 0.20
		5.9174(5)	0.060(8)	0.10 ± 1.31
		6.03537(4)	0.864(8)	0.20 ± 0.09
		6.0907(6)	0.053(8)	0.94 ± 1.50
		6.3131(2)	0.175(8)	0.20 ± 0.45
NGC 1960 91	115559630	0.08866(6)	0.61(1)	0.08 ± 0.16
		2.4550(1)	0.39(1)	0.27 ± 0.25
		2.4935(2)	0.16(1)	0.77 ± 0.61
		2.54095(8)	0.55(1)	0.36 ± 0.20
		2.5952(2)	0.18(1)	0.76 ± 0.56
		2.630129(1)	2.86(1)	0.49 ± 0.03
		2.718156(1)	4.38(1)	0.71 ± 0.02
		2.78065(8)	0.50(1)	0.80 ± 0.20
		2.8577(3)	0.12(1)	0.68 ± 0.83
		3.1156(2)	0.25(1)	0.11 ± 0.38
		5.1705(3)	0.14(1)	0.29 ± 0.70
		5.2317(3)	0.14(1)	0.36 ± 0.73
		5.3221(1)	0.32(1)	0.43 ± 0.32
		5.3566(3)	0.14(1)	0.70 ± 0.69
		5.43484(4)	0.89(1)	0.59 ± 0.11
		5.5002(2)	0.20(1)	0.64 ± 0.51
		5.5642(4)	0.11(1)	0.67 ± 0.89
		5.6842(3)	0.15(1)	0.09 ± 0.64
		5.7456(3)	0.14(1)	0.83 ± 0.70
		5.8340(4)	0.10(1)	0.19 ± 0.94
		8.0266(4)	0.10(1)	0.27 ± 0.95
		10.69714(1)	0.35(1)	0.21 ± 0.27
		10.9122(2)	0.21(1)	0.27 ± 0.47
		16.0053(8)	0.05(1)	0.33 ± 1.98
		16.1415(7)	0.06(1)	0.09 ± 1.69
NGC 1960 138	115642245	0.93352(4)	0.72(8)	0.84 ± 0.11
		1.2550(2)	0.15(8)	0.96 ± 0.53
		1.8663(2)	0.19(8)	0.59 ± 0.42
		2.8764(1)	0.27(8)	0.48 ± 0.29
		2.9804(4)	0.09(8)	0.48 ± 0.88
		3.1401(2)	0.13(8)	0.05 ± 0.61
		4.6486(4)	0.77(8)	0.98 ± 1.02
		4.9161(2)	0.13(8)	0.28 ± 0.60

Table B3. Frequency, period, amplitude and phase of the 14 significant peaks used to fit the period spacing patterns of NGC 1960 81. The dashed empty rows indicate where a gap was identified. The first nine rows are the values of the low-period pattern, and the last nine are for the high-period pattern.

	f [d^{-1}]	P [d]	A [mmag]	ϕ
Group 1	4.4356(5)	0.22544(4)	0.08(1)	0.45 ± 2.21
	–	–	–	–
	3.6128(4)	0.27679(5)	0.11(1)	0.55 ± 1.65
	3.2573(2)	0.30700(4)	0.16(1)	0.09 ± 1.16
	3.0144(2)	0.33174(3)	0.23(1)	0.40 ± 0.79
	2.8523(1)	0.35059(2)	0.35(1)	0.39 ± 0.51
	–	–	–	–
	2.6838(3)	0.37261(7)	0.14(1)	0.85 ± 1.27
	2.5905(2)	0.38602(7)	0.16(1)	0.36 ± 1.10
Group 2	1.80555(5)	0.55386(2)	0.73(1)	0.40 ± 0.16
	1.72538(7)	0.57955(3)	0.57(1)	0.56 ± 0.20
	1.6442(1)	0.60844(5)	0.37(1)	0.15 ± 0.31
	1.5765(2)	0.6343(1)	0.15(1)	0.52 ± 0.76
	–	–	–	–
	1.47028(3)	0.68038(2)	1.34(1)	0.60 ± 0.08
	1.4023(2)	0.7139(1)	0.17(1)	0.58 ± 0.67
	–	–	–	–
	1.2915(1)	0.77516(6)	0.44(1)	0.21 ± 0.26